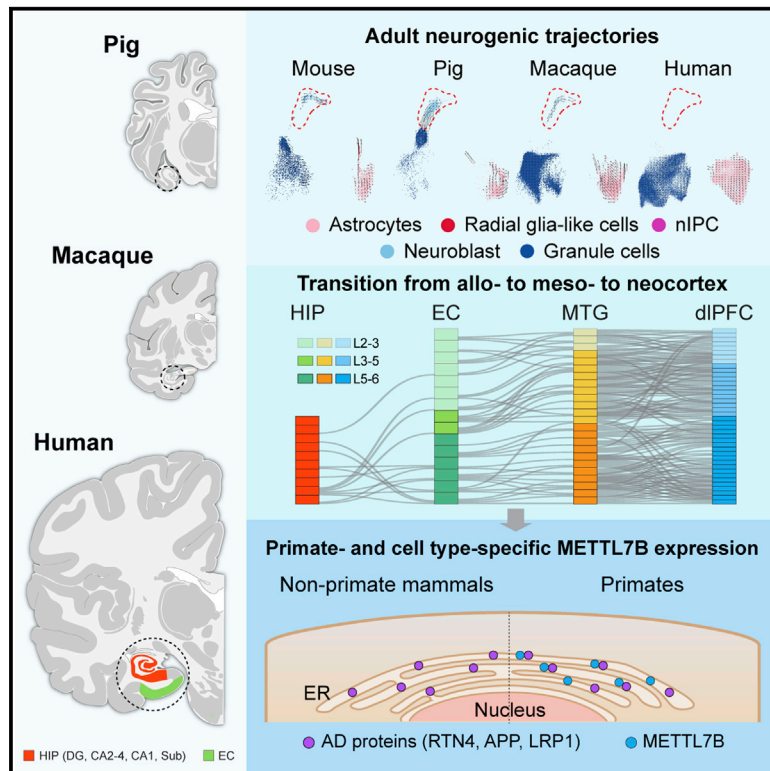


Transcriptomic taxonomy and neurogenic trajectories of adult human, macaque, and pig hippocampal and entorhinal cells

Graphical abstract



Authors

Daniel Franjic, Mario Skarica, Shaojie Ma, ..., Andre M.M. Sousa, Pasko Rakic, Nenad Sestan

Correspondence

nenad.sestan@yale.edu

In brief

Using snRNA-seq of the adult human, macaque, and pig hippocampal-entorhinal system, Franjic et al. defined shared and divergent cell type features, like primate-specific expression of *METTL7B* in some excitatory neurons and astrocytes. They also identified robust transcriptomic and histologic signatures of neurogenesis in the mouse, pig, and macaque but not humans.

Highlights

- Single-nucleus RNA-seq of adult hippocampal-entorhinal cells in human, monkey, and pig
- Transcriptomic signatures of adult neurogenesis in mouse, pig, and monkey but not human
- Excitatory neuron diversification delineates transitions from 3- to 6-layered cortex
- *METTL7B* defines subregion-specific excitatory neurons and astrocytes in primates



Article

Transcriptomic taxonomy and neurogenic trajectories of adult human, macaque, and pig hippocampal and entorhinal cells

Daniel Franjic,^{1,10} Mario Skarica,^{1,10} Shaojie Ma,^{1,2,10} Jon I. Arellano,^{1,10} Andrew T.N. Tebbenkamp,^{1,10} Jinmyung Choi,¹ Chuan Xu,¹ Qian Li,¹ Yury M. Morozov,¹ David Andrijevic,¹ Zvonimir Vrselja,¹ Ana Spajic,¹ Gabriel Santpere,^{1,3} Mingfeng Li,¹ Shupeizhang,¹ Yang Liu,⁴ Joshua Spurrier,⁵ Le Zhang,⁵ Ivan Gudelj,¹ Lucija Rapan,¹ Hideyuki Takahashi,⁵ Anita Huttner,⁶ Rong Fan,⁴ Stephen M. Strittmatter,⁵ Andre M.M. Sousa,^{1,7} Pasko Rakic,^{1,8} and Nenad Sestan^{1,2,8,9,11,*}

¹Department of Neuroscience, Yale School of Medicine, New Haven, CT 06510, USA

²Department of Genetics, Yale School of Medicine, New Haven, CT 06510, USA

³Neurogenomics Group, Research Programme on Biomedical Informatics (GRIB), Hospital del Mar Medical Research Institute (IMIM), DCEXS, Universitat Pompeu Fabra, 08003 Barcelona, Catalonia, Spain

⁴Department of Biomedical Engineering, Yale Stem Cell Center and Yale Cancer Center, and Human and Translational Immunology Program, Yale University, New Haven, CT 06520, USA

⁵Program in Cellular Neuroscience, Neurodegeneration and Repair, Departments of Neurology and of Neuroscience, Yale School of Medicine, New Haven, CT 06536, USA

⁶Department of Pathology, Brady Memorial Laboratory, Yale School of Medicine, New Haven, CT 06510, USA

⁷Waisman Center and Department of Neuroscience, School of Medicine and Public Health, University of Wisconsin-Madison, Madison, WI 53705, USA

⁸Kavli Institute for Neuroscience, Yale School of Medicine, New Haven, CT 06510, USA

⁹Departments of Psychiatry and Comparative Medicine, Program in Cellular Neuroscience, Neurodegeneration and Repair, and Yale Child Study Center, Yale School of Medicine, New Haven, CT 06510, USA

¹⁰These authors contributed equally

¹¹Lead contact

*Correspondence: nenad.sestan@yale.edu
<https://doi.org/10.1016/j.neuron.2021.10.036>

SUMMARY

The hippocampal-entorhinal system supports cognitive functions, has lifelong neurogenic capabilities in many species, and is selectively vulnerable to Alzheimer's disease. To investigate neurogenic potential and cellular diversity, we profiled single-nucleus transcriptomes in five hippocampal-entorhinal subregions in humans, macaques, and pigs. Integrated cross-species analysis revealed robust transcriptomic and histologic signatures of neurogenesis in the adult mouse, pig, and macaque but not humans. Doublecortin (DCX), a widely accepted marker of newly generated granule cells, was detected in diverse human neurons, but it did not define immature neuron populations. To explore species differences in cellular diversity and implications for disease, we characterized subregion-specific, transcriptomically defined cell types and transitional changes from the three-layered archicortex to the six-layered neocortex. Notably, METTL7B defined subregion-specific excitatory neurons and astrocytes in primates, associated with endoplasmic reticulum and lipid droplet proteins, including Alzheimer's disease-related proteins. This resource reveals cell-type- and species-specific properties shaping hippocampal-entorhinal neurogenesis and function.

INTRODUCTION

The hippocampal formation (HIP) and entorhinal cortex (EC) are critical components of a widespread neural network for memory and integration of space and time (Gloor, 1997; Andersen, 2007; Buzsáki and Moser, 2013) and are selectively vulnerable in Alzheimer's disease (AD). Based on cytoarchitectonic, cellular, and circuit-related features, the hippocampal-entorhinal system can be divided into subregions that include the simpler three-layered allocortex of the dentate gyrus (DG), hippocampus proper (*cornu ammonis* [CA]), and subiculum (Sub) and the

more complex laminated periallocortex (mesocortex) of the pre- and parasubicular areas and the EC (Freund, 2002; Suzuki and Amaral, 2004; Klausberger and Somogyi, 2008). The molecular basis of cell type diversity in these subregions and their homology with bordering neocortical cell types remains poorly understood (Kriegstein and Connors, 1986; Hoogland and Vermeulen-Vanderzee, 1989; Reiner, 1991; Ishizuka, 2001; Zeisel et al., 2015; Cembrowski et al., 2016b; Mercer and Thomson, 2017; Shepherd and Rowe, 2017). Laminal organization and cytoarchitecture changes gradually from allocortex to neocortex sectors across this region. Histological, physiological, and



connectional studies suggest that the allocortex is composed of glutamatergic excitatory projection neurons that resemble those in the deep layers of the mammalian neocortex (Kriegstein and Connors, 1986; Reiner, 1991; Ishizuka, 2001; Luzzati, 2015; Shepherd and Rowe, 2017).

Neurogenesis of granule cells in the adult DG has been documented across mammalian species (Patzke et al., 2015) and studied extensively in rodents, propelling a number of hypotheses about its functional role in cognitive processes and its potential for regenerative approaches. Adult neurogenesis also persists in non-human primates, but at substantially lower levels than in rodents (Gould et al., 1998; Kornack and Rakic, 1999; Ngwenya et al., 2006; Jabès et al., 2010; Kohler et al., 2011; Yuan et al., 2014). However, there is no consensus regarding the existence of significant neurogenesis in the adult human DG. Previous studies have provided evidence of generation of granule cells in the adult and aged human DG through detection of cell proliferation (Eriksson et al., 1998; Spalding et al., 2013). Other studies have reported varied amounts of cells expressing doublecortin (DCX; a widely adopted marker of neuroblasts and immature neurons) in the adult human DG (Knoth et al., 2010; Boldrini et al., 2018; Moreno-Jiménez et al., 2019; Tobin et al., 2019). Similarly, bulk tissue RNA sequencing shows expression of DCX in the adult and aged human HIP, albeit dramatically lower than in the developing human or adult macaque HIP (Kang et al., 2011; Sousa et al., 2017; Zhu et al., 2018). Conversely, other studies have failed to identify neural progenitors or DCX-expressing neuroblasts after childhood in human DG samples (Dennis et al., 2016; Cipriani et al., 2018; Sorrells et al., 2018; Seki et al., 2019). Recently, single-cell RNA sequencing has been applied to characterize the process of DG neurogenesis at developmental and adult stages in mice, revealing the gene expression cascades along the granule cell lineage, from radial glia-like (RGL) cells to neural intermediate progenitor cells (nIPCs), to neuroblast cells, to granule cells, (Hochgerner et al., 2018). This technique is well suited to bridge histologic and genetic analyses of cell lineage subtypes and possibly resolve the controversy surrounding human adult neurogenesis (Kempermann et al., 2018; Kuhn et al., 2018; Lee and Thuret, 2018; Paredes et al., 2018; Abbott and Nigusie, 2020).

Within the human hippocampal-entorhinal system, some cell types and circuits are selectively vulnerable to certain pathological processes, including ischemia or AD pathology and age-related neuronal loss (Schmidt-Kastner and Freund, 1991; Braak and Del Tredici, 2015). Given this selectivity, more detailed molecular and cellular profiling of this system will aid our understanding of the human brain and neuropsychiatric disease.

To investigate key cell-type- and species-specific differences in gene expression, neurogenic capacity, and variable disease susceptibility, we performed high-coverage single-nucleus RNA sequencing (snRNA-seq) on five anatomically defined subregions of the hippocampal-entorhinal system from adult human donors (DG, CA2–CA4, CA1, Sub, and EC). We also profiled DG cell populations from adult rhesus macaques (*Macaca mulatta*) and all hippocampal fields from young adult pigs (*Sus scrofa*). Similar to recent snRNA-seq studies of the postmortem adult human hippocampal-entorhinal system (Habib et al., 2017; Grub-

man et al., 2019; Ayhan et al., 2021; Leng et al., 2021), these findings identify highly diverse cell populations with clear regional distinctions. Additionally, we investigated underlying species-level distinctions within this region by cross-species integrative comparisons with parallel samples from young adult mice (*Mus musculus*) (Hochgerner et al., 2018), supporting higher-order inferences relative to evolution, behavior, and disease. This interactive resource is accessible at <http://resources.sestanlab.org/hippocampus>.

RESULTS

Transcriptomic diversity of adult human hippocampal and entorhinal cells

We used snRNA-seq to profile five subregions (DG, CA2–CA4, CA1, Sub, and EC) microdissected from fresh-frozen postmortem brains of clinically unremarkable adult human donors (age, 53 ± 5 years; postmortem interval [PMI], 15.6 ± 2.0 h of mostly cold ischemic time; 2 females and 4 males; Figures 1A–1D; Table S1). Unbiased isolation of nuclei using our modified protocol (Li et al., 2018; Zhu et al., 2018) followed by single nucleus RNA (snRNA) barcoding, cDNA sequencing, and quality filtering yielded 219,058 high-quality single-nucleus profiles (Figures 1A–1D and S1A–S1C). Expression patterns of major cell type markers identified 69,461 neurons ($35.7\% \pm 4.1\%$) and 149,597 ($64.3\% \pm 4.1\%$) non-neuronal cells (NNCs) (Figures 1B–1D and S1D). Within neurons, there were 55,888 ($77.8\% \pm 2.8\%$ of all neurons) glutamatergic excitatory neurons (ExNs) and 13,542 ($22.1\% \pm 2.8\%$) GABAergic inhibitory neurons (InNs), proportions that varied substantially between regions (Figure S1C).

Iterative clustering identified 69 transcriptomically distinct cell clusters across all donors (Figures 1B–1D) that were organized into a dendrographic taxonomy reflecting their unique gene expression patterns. This revealed 25 ExN subtypes, 23 InN subtypes, a Cajal Retzius-like cell type, and 20 NNC subtypes (Figures 1E, S1E, and S1F), which were all broadly mapped to those defined previously in the adult human hippocampus (Figures S1G and S1H), where subregions were not selectively dissected (Habib et al., 2017; Ayhan et al., 2021). Within ExN subtypes, apart from the expected transcriptomic diversity following the cytoarchitectonic organization of the HIP and EC (Figure 1E), we found marked heterogeneity in the molecular profiles within regions, indicating a finer molecular subdivision than the apparent cytoarchitecture. For example, in the DG, we found two distinct subclusters of *PROX1*-expressing granule cells, characterized by expression of *PDLIM5* and *SGCZ*, respectively (Figure S1F). Similar population diversity was identified in CA1, CA2–CA4, and Sub (Figures 1E and S1F), matching those described previously (Nielsen et al., 2010; Slomianka et al., 2011; Cipriani et al., 2016; Cembrowski et al., 2018; Cembrowski et al., 2016a, 2016b). Within the EC, ExNs exhibited much more diversity than the expected division by laminar features, and we identified neuron subtypes marked by layer 2/3 markers (*CUX2* and *RELN*) or deep layer markers (*TLE4*, *ADRA1A*, and/or *THEMIS*).

In contrast to ExNs, InN and NNC types were distributed more uniformly, without significant transcriptomic diversity across regions (Figure 1E). InN subtypes were distinguished by major markers (*SST*, *PVALB*, *VIP*, and *LAMP5*), and NNC populations

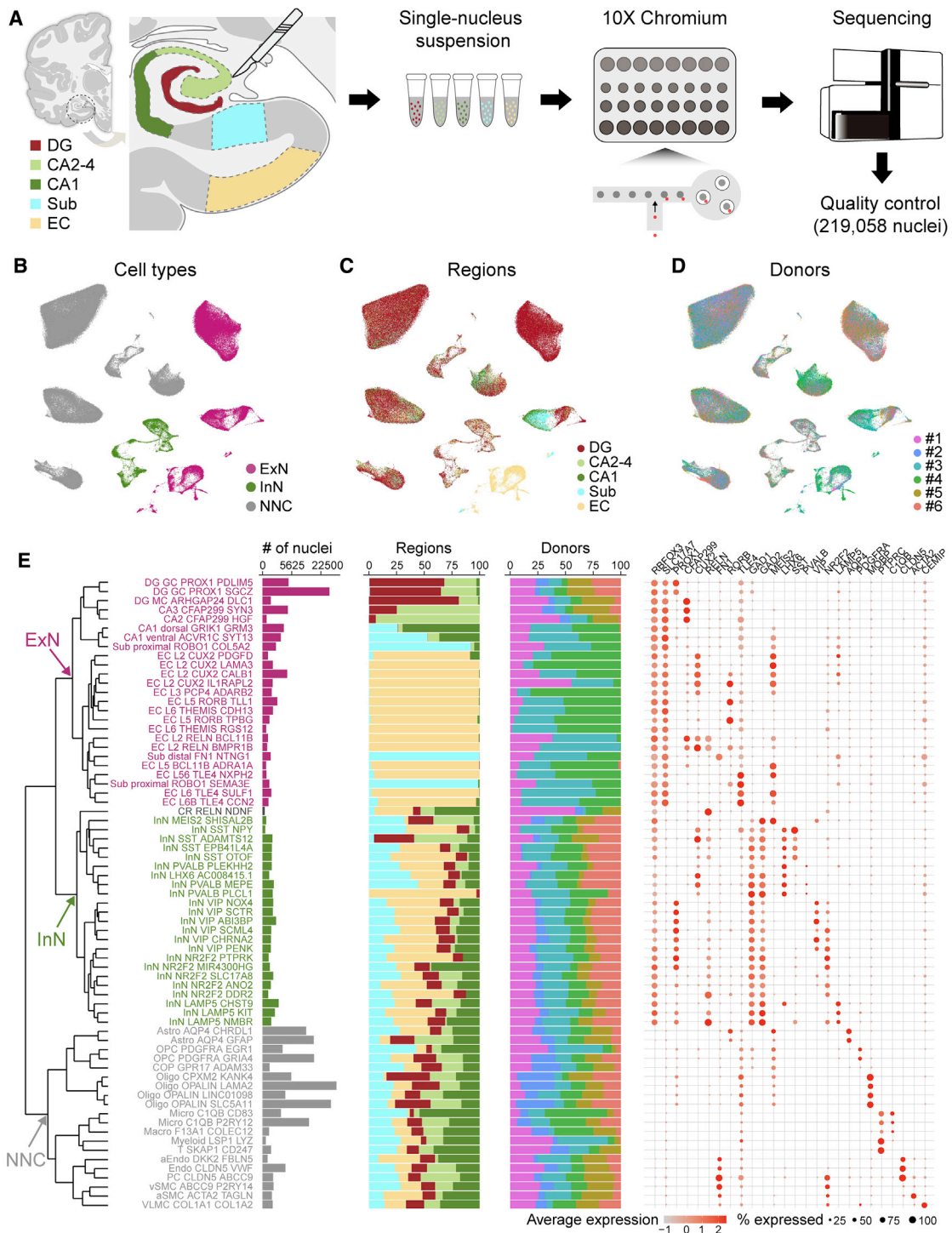


Figure 1. Cell type diversity in the human hippocampal-entorhinal system revealed by snRNA-seq

(A) Schematic of the analytic workflow.

(B–D) UMAP visualization of all nuclei, colored by major cell types (B), subregions (C), and donors (D).

(E) Dendrogram depicting the hierarchical taxonomy across all cell subtypes. Bar plots show the number of nuclei and relative subregional and donor contributions, with the coloring scheme conforming to (B)–(D). The dot plot shows the expression of marker genes. GC, granule cell; MC, mossy cell; Astro, astrocyte; OPC, oligodendrocyte precursor cell; COP, committed OPC; Oligo, oligodendrocyte; Micro, microglia; Macro, macrophage; Myeloid, myeloid cell; T, T cell; aEndo, arterial endothelial cell; PC, pericyte; vSMC, venous smooth muscle cell; aSMC, arterial smooth muscle cell; VLMC, vascular and leptomeningeal cell. See also Figure S1.

included astrocytes, oligodendrocyte precursor cells, oligodendrocytes, microglia, and vasculature cells.

These data present high-resolution cell populations extending previous findings outlining the functional cell diversity in the human hippocampal-entorhinal system (Freund, 2002; Suzuki and Amaral, 2004; Klausberger and Somogyi, 2008), which now enables detailed investigation of fundamental features of this system.

snRNA-seq reveals a neurogenic trajectory in the macaque, pig, and mouse DG that is virtually absent in humans

To ensure a robust analytic power to detect transcriptomic signatures of adult neurogenesis (Table S2), we collected 139,187 DG nuclei from 6 adult human donors (Figure S2A; Table S1; STAR Methods), each with 1–8 technical replicates. We also generated snRNA-seq data from adult rhesus macaques as a reference for neurogenesis in the primate lineage and from young adult pigs (Table S1) as a control for the PMI effect because they were analyzed at 30 min, 1 h, and 7 h of warm ischemic PMI. To take full advantage of the inter-species information, we integrated our human, macaque, and pig DG data with published single-cell RNA-seq data from the young adult mouse DG (Hochgerner et al., 2018), an established animal model with robust adult neurogenesis, to screen for neurogenic cells as well as *DCX* expression in these species. The integration revealed a broad cell type matching across species (Figures 2A, S2B, and S2C) and showed that RGL cells clustered with astrocytes because they share expression of multiple astrocyte markers (Figure 2A; Bonaguidi et al., 2011; Hochgerner et al., 2018; Arellano et al., 2021). Homologs of mouse nIPCs and neuroblasts were robustly observed in the pig and macaque but not humans, even though we profiled 25 times more cells in humans and were able to detect *DCX* transcripts in all human DG samples (Figures 2A and S2A).

Reintegration with only the granule cell lineage and astrocytes confirmed the alignment and unveiled a clearer trajectory from nIPC to neuroblast to granule cell in the mouse, pig, and macaque but not humans (Figure 2B). Those variations among species were recapitulated via RNA velocity (Figure 2B), which infers cell differentiation lineage by leveraging splicing dynamics (Bergen et al., 2020). To more rigorously identify human cells matching expression profiles of homolog nIPCs and neuroblasts, we used Seurat and Harmony (Korsunsky et al., 2019; Stuart et al., 2019) to perform pairwise integration between humans and each of the other species. Summarizing all integrations, we found a total of 20 cells located in the vicinity of homolog progenitors and neuroblast cells in humans (Figures 2C and S2D).

However, allocation in the domain of homolog progenitors and neuroblasts per se does not imply neurogenic identity because multiple factors, such as low cell quality, interspecies differences, and method-specific bias, may contribute to the misplacement. To assess the identity of these cells and the change of signatures delineating granule cell differentiation across species, we obtained subtype marker genes in the mouse, pig, and macaque. Expression patterns of these markers confirmed the alignment of homolog progenitors and neuroblasts across species (Figures S2E and S2F) and identified markers shared in at least two species. These include multiple

cell cycle genes in nIPCs (e.g., *TOP2A*, *CENPF*, and *MKI67*) and some common neuroblast markers (*DCX* and *CALB2*) in neuroblasts (red gene labels, Figures 2C and S2G). The shared neuroblast markers also included *ST8SIA2* (red gene labels, Figure S2G), a gene encoding a polysialyltransferase that polysialylates NCAM to produce PSA-NCAM (Angata et al., 2002), which is also considered a marker of neuroblasts and immature neurons (Seki et al., 2019). However, some shared markers showed distinct patterns in humans, with very high expression in mature granule cells (Figure S2G). Moreover, multiple markers exhibited distinct patterns across species (e.g., *NEUROD4* and *DUSP14*; blue gene labels, Figure 2C), suggesting that transcriptomic neurogenic signatures are not fully preserved across species and that defining cell identity should be done with caution.

Next we sought to screen for the presence of these transcriptomically defined markers along with other traditional progenitor and neuroblast markers in the adult human DG (Hochgerner et al., 2018; Berg et al., 2019). Among the 20 human cells clustered with homolog progenitors and neuroblast cells in the uniform manifold approximation and projection (UMAP) space, we observed extremely low expression for most of the markers and expression comparable with background granule cells for the rest (Figure 2C). There is only one cell showing neuroblast features characterized by co-expression of *PROX1*, *DCX*, *CALB2*, *NEUROD6*, and *DPYSL3* (blue arrow, Figure 2C). We also recognized one putative nIPC in humans co-expressing *PROX1* and several nIPC markers (cell indicated by a red arrow, Figure 2C), including *TOP2A*, *CENPF*, and *MKI67*. Unbiased co-expression searching only revealed one additional *PROX1*-expressing granule cell co-expressing these neuroblast markers (*DCX*, *CALB2*, and *DPYSL3*) in humans (Figures S2G and S2H). Still, this gene profile was not specific enough to define putative neuroblasts because high co-expression of these 3 putative neuroblast markers and *PROX1* was observed in lNns, especially in humans.

Because neuroblasts at later stages of maturation may possess a combination of progenitor and mature granule cell signatures reminiscent of the doublet features, we further incorporated the previously removed doublets into the human-mouse integrative analysis. Only a few human cells aligned with the mouse neuroblast subtype (Figure S2I), and their expression profiles were suggestive of glia or mature neuron or neuron/glia doublets but not neurogenic cells (Figure S2J). Considering that human prenatal and adult neuroblast cells may share transcriptomic similarity, as observed in the mouse (Hochgerner et al., 2018), we further projected adult human DG data to fetal human DG data (Zhong et al., 2020). Again, no clear granule cell trajectory or cells expressing nIPC or neuroblast markers were detected in adult humans (Figures S2K and S2L). Our exhaustive integrative cross-species analysis identified clear and robust trajectories for adult neurogenesis in mouse, pig, and macaque, but not in humans. We only identified one cell with a transcriptomic profile consistent with neuronal progenitors and one cell with a profile consistent with neuroblasts among 139,187 DG cells (0.0007% for each cell) and 32,067 granule cells (0.003% for each cell), a ratio substantially lower than previous estimations based on *DCX* protein expression and ^{14}C incorporation analysis, which suggested a range of 28–1,218 neuroblasts for our sample size (see Table S2 for details).

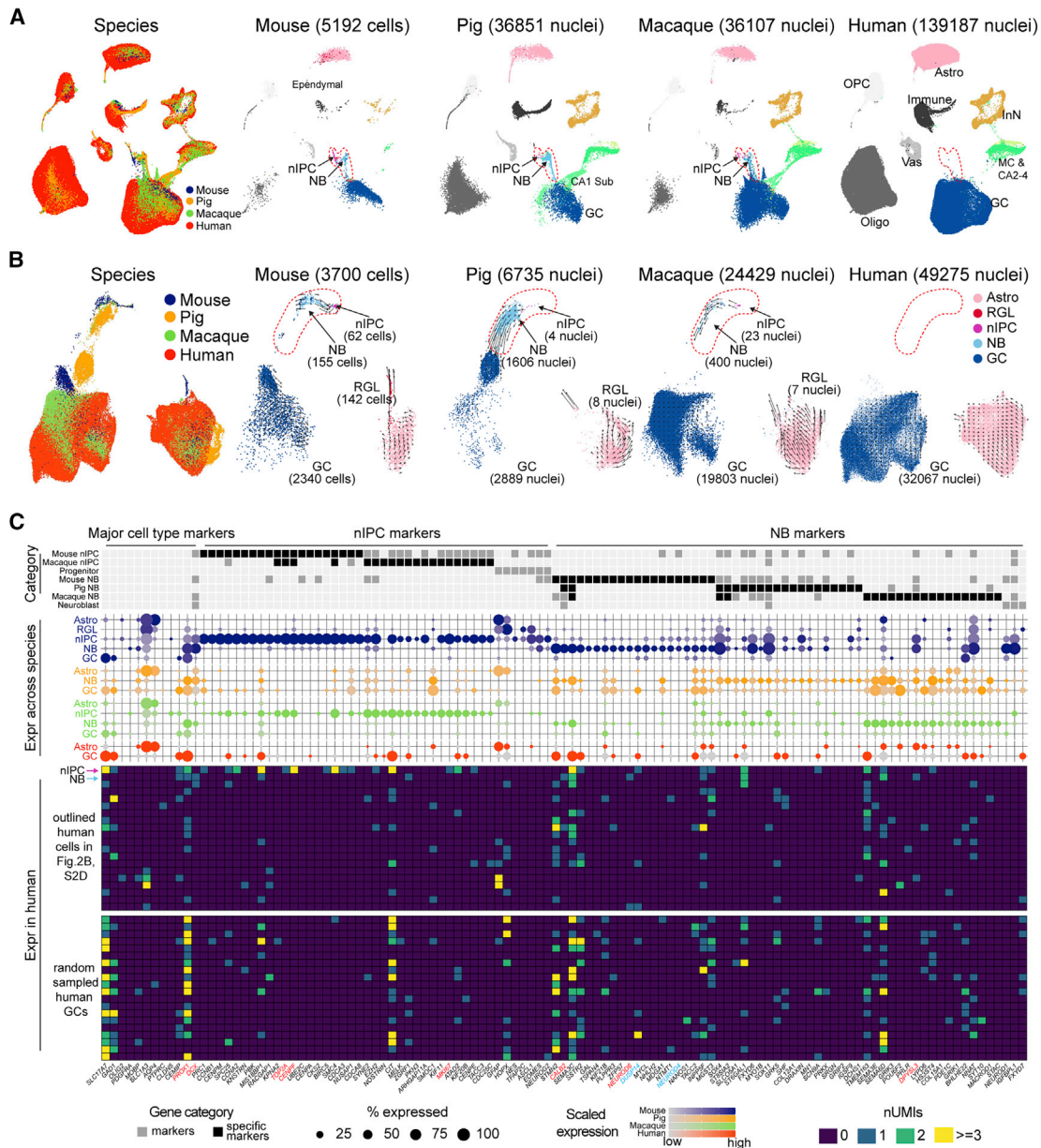


Figure 2. Cross-species analysis of transcriptomic signatures of adult neurogenic trajectories

(A and B) Seurat integration of all DG cells (A) or only astrocytes (Astro) and the granule cell (GC) lineage (B) across species. In (B), arrow directions and lengths are correlated with cell differentiation paths and speed, respectively.

(C) Expression of cluster markers across species. The categories “progenitor” and “neuroblast” were annotated manually (Hochgerner et al., 2018; Berg et al., 2019). Center: dot plot depicting the expression of the markers, with dots colored by species. Bottom: marker expression in the 20 human cells residing in the nIPC and neuroblast domain as well as the randomly sampled human GCs. The first two rows highlighted by arrows represent the two putative human neurogenic cells. RGL, radial glia-like cells; nIPC, neural intermediate progenitor cell; NB, neuroblasts. CA2–CA4, CA2–CA4 ExNs; CA1 Sub, CA1 and Sub ExNs.

See also Figure S2 and Table S2.

DCX RNA is not a specific marker of neuroblasts or immature granule neurons

To further investigate the neurogenic potential, we profiled *DCX* RNA expression across species. Datasets from the four species were down-sampled to the same sequencing depth to have comparable metrics (STAR Methods). This revealed comparable

magnitudes of *DCX* expression levels and similar expression patterns across species but selective enrichment in mouse neuroblasts and, to a lesser extent, in pig and macaque neuroblasts (Figure 3A). Importantly, *DCX* expression with at least one unique molecular identifier (UMI) was found in granule cells across species, with humans showing the scarcest expression (mouse,

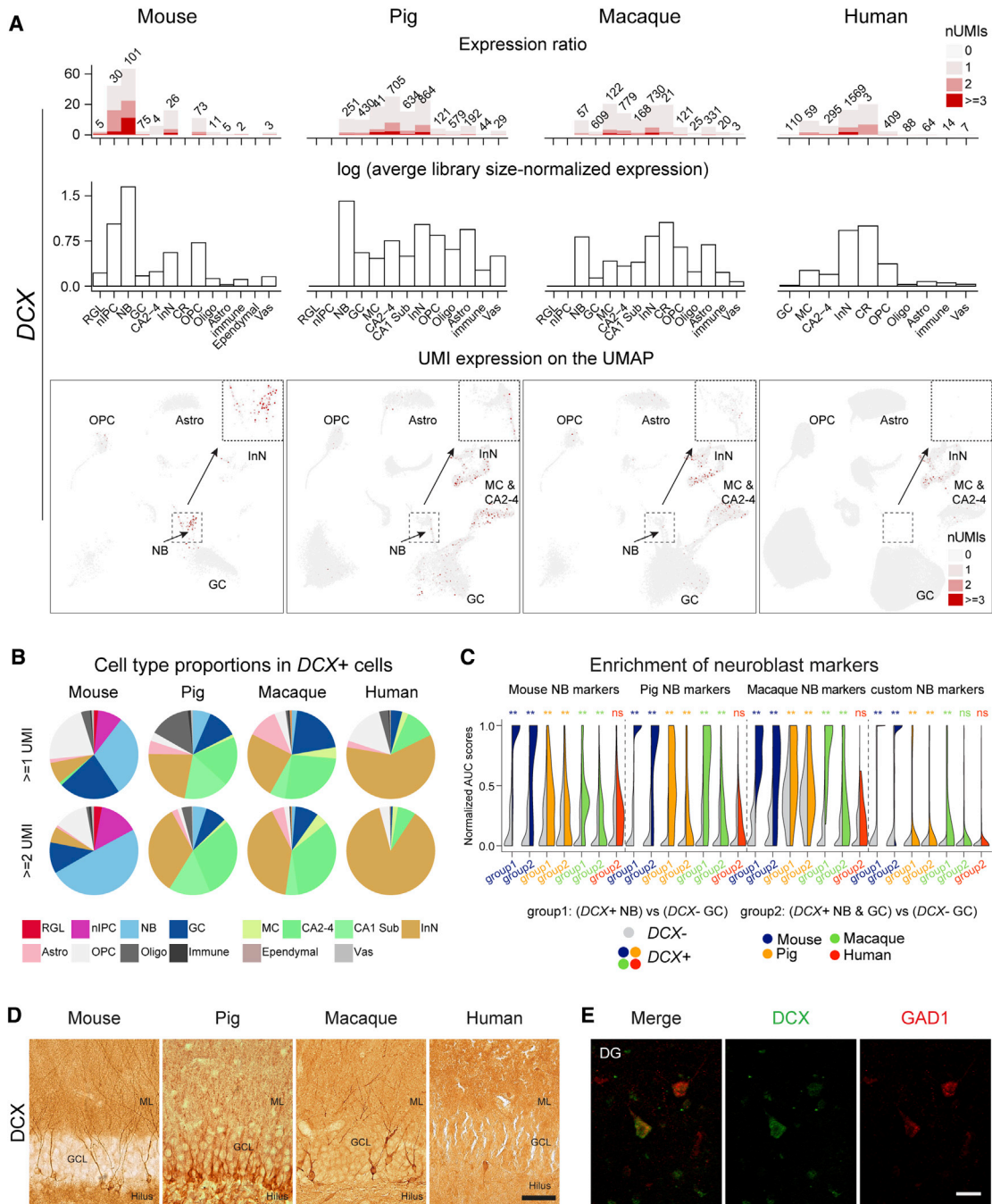


Figure 3. Hippocampal *DCX* expression across species

(A) Top: the numbers (text label) and percentages (y axis) of cells expressing *DCX*. Center: average library size-normalized expression of *DCX*. Bottom: *DCX* expression on UMAP, with insets highlighting the NB domain.

(B) Cell type proportions of *DCX*-expressing cells across species.

(C) Enrichment of different sets of NB markers in *DCX*+ compared with *DCX*- cells. Significance was tested using one-tailed Wilcoxon rank-sum test (** $p < 0.01$; ns, not significant).

(D) Images of the mouse, pig, macaque, and human DG immunolabeled against *DCX*. The scale bars represent 50 μ m (mouse, pig, and macaque) and 75 μ m (human). GCL, granular cell layer; ML, molecular layer.

(E) Colocalization of *DCX* and *GAD1* in one cell with InN morphology in the molecular layer of the human DG. Scale bar, 30 μ m.

See also [Figure S3](#) and [Table S3](#).

3.21%; pig, 14.88%; rhesus macaque, 3.08%; human, 110 of 32,067 or 0.34%) (Figure 3A; Table S3). However, one UMI is a low baseline that could represent background and does not reliably confer cell identity (Figure S1D). Accordingly, we compared *DCX* expression of at least 2 UMIs and found a similar pattern, still with humans showing the scarcest expression (mouse, 0.51%; pig, 1.97%; rhesus macaque, 0.2%; human, 4 of 32,067 or 0.01%; Table S3). Conversely, prominent *DCX* expression was detected in non-granule cells, especially in InNs, where 7.28% expressed at least 2 *DCX* UMIs (Figure 3A; Table S3), suggesting that low expression, rather than low detection, is the explanation for the scarce presence of *DCX* in human granule cells. Although human samples overall have a longer PMI (Table S1), this clear expression of *DCX* indicates that the long PMIs do not limit detection of *DCX* transcripts. Nonetheless, we further evaluated the effect of PMI by performing snRNA-seq analysis in pig brains with PMI of 30 min, 1 h, and 7 h. Pig brains were kept at room temperature (warm PMI), while human specimens used in our study spent typically less than 4 h at room temperature (warm PMI) before they were refrigerated (cold PMI) to slow down tissue and cell deterioration until autopsy. The longer warm PMI in pig brains is likely to exacerbate the effect of the postmortem interval compared to cold preserved brains, but the results showed comparable *DCX* expression and similar abundance of neural progenitors and neuroblasts in all three conditions, once again suggesting that PMI might not be a substantial factor influencing RNA preservation and/or detection (Figure S3C). Similar to humans, *DCX* expression outside of the neuroblast/granule cell population was detected in all analyzed species, but it was more prominent in the pig and primates than in mice (Figure 3B). These results suggest that *DCX* expression per se is inadequate to define adult neurogenesis.

To further interrogate whether the 110 *DCX*-expressing human granule cells might be neuroblasts, we tested whether they were enriched in neuroblast markers compared with *DCX*-negative granule cells. Our results showed lack of enrichment in neuroblast markers (Figure 3C), a pattern that persists in the original human data with higher depth prior to down-sampling (Figure S3B). This result was in stark contrast with the mouse, pig, and macaque, which showed conserved enrichment of neuroblast markers in *DCX*-expressing granule cells, ratifying the robustness of the method to detect potential neuroblasts overriding species differences. This result further confirms the absence of a detectable neurogenic trajectory in our human DG samples, revealed by the integrative analysis, and suggests that mature granule cells express some degree of *DCX* in the adult human DG, similar to other mature neuronal populations.

We complemented these snRNA-seq analyses using immunohistochemistry with two different commonly used antibodies against *DCX* on the hippocampus of young adult mouse and pig, and adult rhesus macaque and human. Mice, pigs, and macaques exhibited numerous *DCX*-immunolabeled (*DCX*-IL) cells in the DG with immature and mature granule cell morphology (Figure 3D), as reported previously (Guidi et al., 2011; Jabès et al., 2010; Seki, 2002). In humans, we tested a cohort of 10 cases (Table S3) where the HIP and EC or amygdala were available. We screened the amygdala as an internal control for *DCX* detection because it harbors a large population of cells strongly immunola-

beled with both *DCX* antibodies in the paralaminar nucleus (Sorrells et al., 2019). To maximize detection, we used several protocols for antigen retrieval, including one used in previous studies (Moreno-Jiménez et al., 2019; Flor-García et al., 2020). However, we did not see significant differences between the protocols. With standard citrate buffer antigen retrieval, we could detect numerous reliably immunolabeled cells in the amygdala of all cases, occasional and scarcer *DCX*-IL cells in the EC and perirhinal cortex, and rare *DCX*-IL cells in the Sub and CA fields of some cases (Table S3). Although *DCX*-IL cells in the amygdala and EC showed strong labeling in the somata and processes, in the DG we only found some lightly *DCX*-IL cells, located mostly in the molecular layer or in the subgranular zone (SGZ) and hilus and occasionally within the granule cell layer (Figures 3D, S3D–S3G and S3M–S3Q). However, their morphology and localization were more consistent with GABAergic InNs than with immature granule cells, and, in fact, some of them were lightly labeled with GAD1, a marker of InNs (Figures 3E and S3M–S3R). These results are consistent with our snRNA-seq analysis. Similar lightly labeled cells were found in other regions, even in pyramidal cells, which also suggests the possibility of background staining (Figures S3D–S3G), although such labeling was not detected in controls lacking the primary antibody. Immunostaining against PSA-NCAM, a selective marker of neuroblasts and immature neurons in the DG of rodents (Seki, 2002), showed a completely different pattern of staining in the human, labeling numerous cells with InN morphology in the DG and hilar area (Figure S3H), as shown previously (Mikkonen et al., 1998; Seki et al., 2019), that matched the predominant distribution outside of the typical neurogenic lineage seen for *DCX* transcripts. We did not colocalize those markers because anti-*DCX* antibodies require antigen retrieval, and anti-PSA-NCAM immunostaining does not tolerate the same treatment.

The possible effect of the PMI in the human samples did not preclude *DCX* detection because we could detect *DCX*-IL cells in the amygdala and EC/perirhinal cortex in cases with up to 24 h of mostly cold ischemic PMI. Additionally, we evaluated the effect of PMI in the pig DG with 15 and 24 h of cold ischemic PMI and in a macaque with a 16 h of cold ischemic PMI using immunohistochemistry (Figures S3I–S3L; Table S3). In both cases, there was a reduction in the number of *DCX*-IL cells, some of which exhibited varicose dendrites (Figures 3D and S3I–S3L). However, these results indicate that long PMIs do not preclude detection of *DCX*-IL cells in the DG or adjacent cortex. Cumulatively, our integrated cross-species snRNA-seq analysis and *DCX* immunohistochemistry revealed clear and robust evidence of adult neurogenesis in our mouse, pig, and macaque but not human tissue samples.

Taxonomic relationship of neural cells across the allo-, meso-, and neocortex

The putative homology between neurons in the hippocampal-entorhinal system and neocortical neurons, and in particular the cytoarchitectonic and evolutionary transition between the allo-, meso-, and neocortex, offers an opportunity to reveal organizational principles underlying the specialization and function of the cerebral cortex. To elucidate these principles, we compared cell profiles across hippocampal-entorhinal subregions and

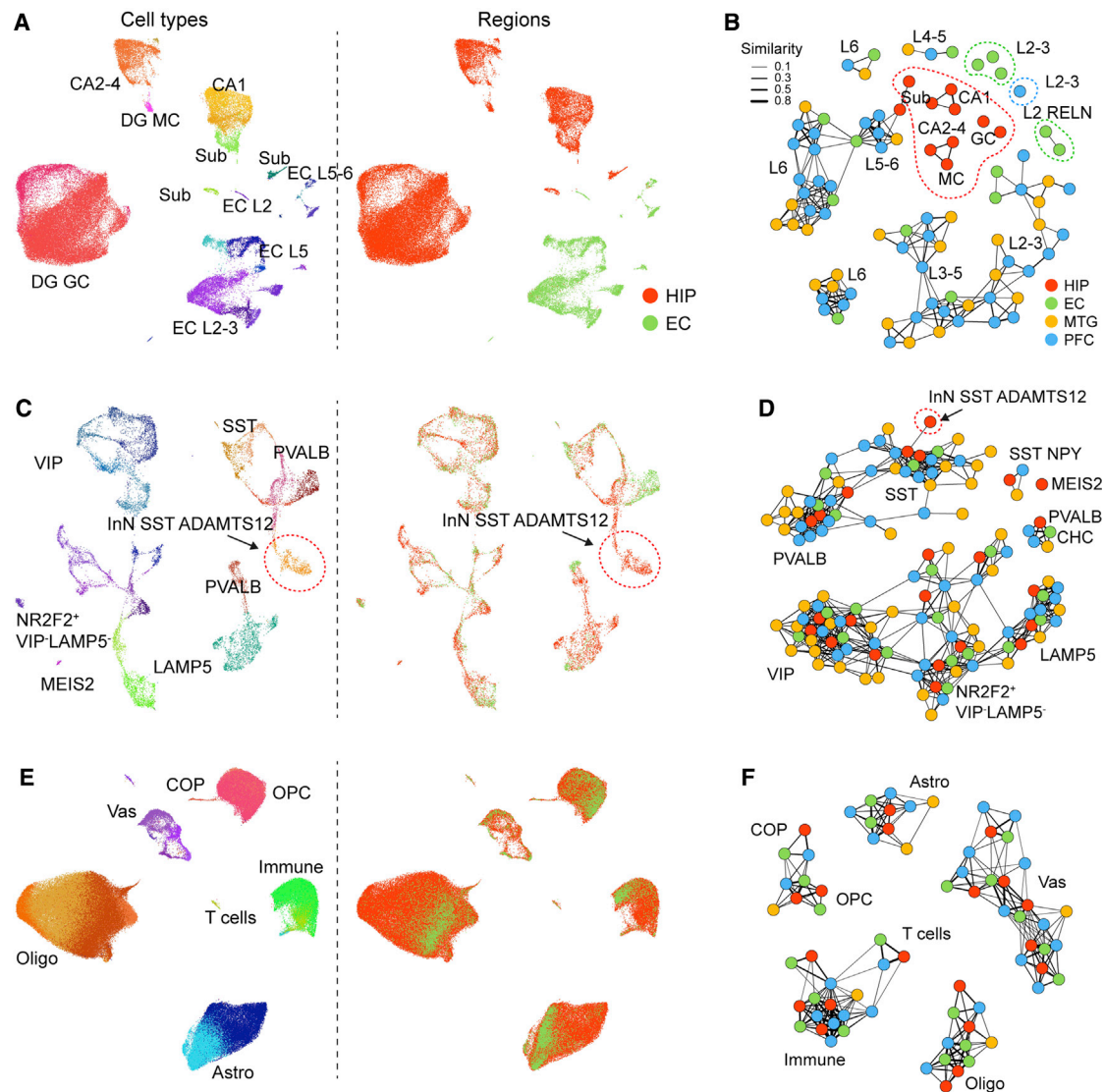


Figure 4. Transcriptomic similarities and differences of hippocampal, entorhinal, and neocortical cell types

(A) Left: UMAP showing all ExN nuclei colored by subtype (left) or region (right). (B) Network demonstrating the extent of transcriptome similarities among ExN subtypes of the HIP, EC, MTG (Hodge et al., 2019), and dIPFC (Li et al., 2018). Dots represent the subtypes within each brain region, and the widths of lines represent the strength of similarity. Subtypes with regional specificity are outlined in corresponding colors. (C–F) As in (A) and (B) for InNs (C and D) and NNCs (E and F). Vas, vascular cell.

transcriptomically defined cell types within two human neocortical regions: the dorsolateral prefrontal cortex (dIPFC/DFC) (Li et al., 2018) and middle temporal gyrus (MTG) (Hodge et al., 2019).

Aside from the marked heterogeneity we observed within each subfield of the HIP (Figure 1E), we also observed a clear distinction between ExNs of the CA fields and Sub compared with those of the EC (Figures 4A and 4B) as well as those of the neocortical MTG and dIPFC. As expected from the laminar structure, we observed higher similarity between ExNs of MTG and dIPFC and, to a lesser extent, between ExNs of the EC and those of the MTG and dIPFC (Figure 4B). In total, we revealed 15 ExN subtypes with regional specificity (three in the DG, two in CA2–CA4,

two in CA1, two in Sub, five in the EC, and one in the dIPFC, as outlined in Figure 4B).

In particular, we found that deep-layer ExN subtypes in the neocortex were well represented in the EC and, to a lesser extent, in the HIP, but upper-layer neuron subtypes were not well represented (Figures 5A and S4A). For example, we identified two EC subtypes with characteristics of layer 2 cells expressing *RELN* that, similar to a previous report (Witter et al., 2017), did not correspond closely to any ExN subtype detected in the neocortex (Figure 4B). Consistent with this observation, all subtypes of HIP ExNs showed higher expression of molecular markers for neocortical deep-layer ExNs than for upper-layer ExNs (Figures S4A and

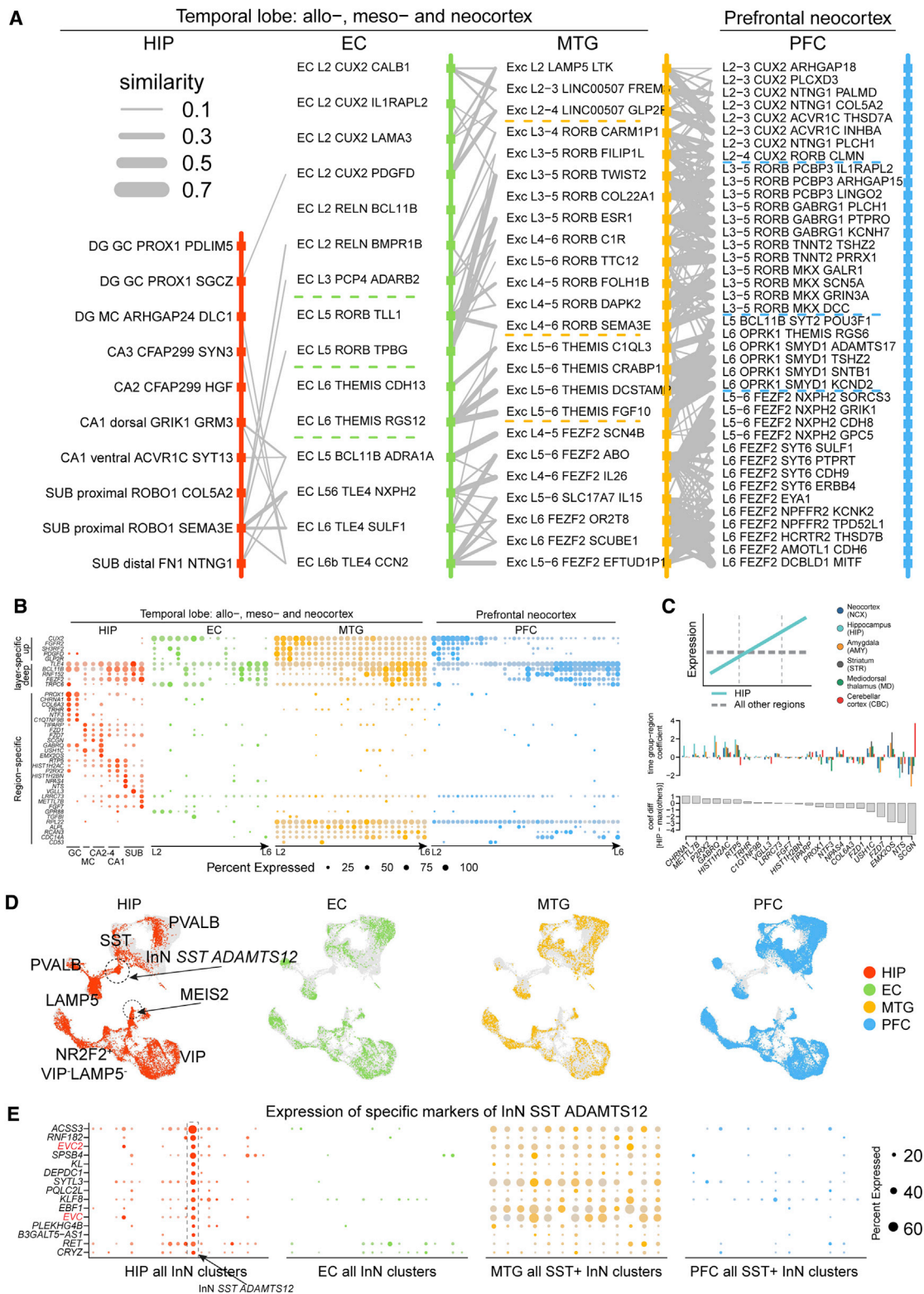


Figure 5. Taxonomic relationships of cell types across the allo-, meso-, and neocortex

(A) Transcriptomic relations across subtypes of pairwise regions, organized according to layer distributions. Broad layer distinction is marked by dotted lines. (B) Expression of neocortical upper-layer and deep-layer markers as well as region-specific genes.

(legend continued on next page)

S4B). Moreover, we observed lower expression of key molecular markers of intracerebral projection neurons in each of the HIP ExN subtypes compared with other neocortical ExN populations (Figure S4C), which likely reflects the restricted and largely ipsilateral telencephalic projections of the human hippocampal subfields to limbic areas (Cenquizca and Swanson, 2007). Nevertheless, there was one DG granule cell subtype that transcriptomically resembled one upper-layer ExN subtype in the EC (Figure 5A), which might recapitulate the similarities found between the HIP and neocortex in the mouse (Yao et al., 2021). We next identified several genes that underlie the molecular specificity of ExNs within the HIP, including *CHRNA1*, *METTL7B*, and *P2RX2*. To gain insight into their potential roles in hippocampal development and maturation, we then examined their temporal expression and found mixed patterns of up- and downregulation (Figure 5C). This suggests that the molecular coordination of hippocampal specification occurs at multiple time points using multiple processes.

In contrast to the observed patterns for ExNs, InNs did not exhibit an obvious transition between the allo-, meso-, and neocortex, with just two HIP InN clusters (InN *MEIS2 SHISAL2B* and InN *SST ADAMTS12*) lacking a clear counterpart in the EC, MTG, and dIPFC (Figures 4C, 4D, and 5D). The former matched to a white matter InN subtype (Frazer et al., 2017; Tasic et al., 2018), and the cell population variations could actually reflect tissue dissection differences. The other cell type, InN *SST ADAMTS12*, was marked by expression of two EvC ciliary complex genes, *EVC* and *EVC2* (Figure 5E), involved in hippocampal ciliary sonic hedgehog signaling (Breunig et al., 2008; Rhee et al., 2016; Park et al., 2019). Last, NNC types constituted the most transcriptomically conserved populations across the allo-, meso-, and neocortical taxonomy, with a high similarity in each subtype across all regions (Figures 4E and 4F). Notably, putative interlaminar astrocytes (Astro *AQP4 GFAP*, layer 1) and protoplasmic astrocytes (Astro *AQP4 CHRDL1*, layers 2–6) (Oberheim et al., 2009; Hodge et al., 2019) were present in all four regions (Figure S4D), which points to the possibility that astrocyte lamination was not a result of the six-layered neocortex in mammals but may be an ancient feature. These findings indicate that ExNs exhibit the most prominent differences across the allo-, meso-, and neocortex, including the increased prevalence of intracerebral projection neurons in the neocortex compared with the allocortex.

Primate age- and cell-type-specific *METTL7B* expression

Among the genes specific to hippocampal ExNs in the transition from allo- to neocortex, we identified *CHRNA1* and *METTL7B* as two genes showing temporal specificity in the adult hippocampus compared with other brain areas along development (Figure 5C). *METTL7B* has been described to be expressed predominantly in enzymatically and metabolically active cells in the

liver (Uhlén et al., 2015) and has not been studied in the vertebrate brain, so we decided to further investigate its possible role in hippocampus biology. *METTL7B* encodes a membrane protein associated with the endoplasmic reticulum (ER) and lipid droplets (LD), and, by amino acid sequence homology, is predicted to belong to the protein methyltransferase superfamily (Turró et al., 2006; Thomas et al., 2013).

We mapped the cell type expression of *METTL7B* across all analyzed species and found *METTL7B* to be only expressed in humans and macaques but not in pigs or mice (Figure 6A). These results were confirmed with bulk tissue RNA-seq, quantitative PCR, and western blot and also using a *lacZ* reporter in the mouse (Figures 6B–6F and S5A). In humans, we observed the highest expression in ExNs, especially in the DG, followed by CA2–CA4 and then Sub and moderate expression in astrocytes (Figure 6A). The same pattern of expression was found in macaques but with higher expression in astrocytes. Immunolabeling of human and macaque hippocampal tissue confirmed these findings (Figures 6G and S5B). Given that there was trace expression in the human MTG (Figure 5B), we surveyed 11 areas of the human neocortex and found high levels in the large pyramidal neurons of layer 5B (Figures S5C and S5D), such as Betz and Meynert cells in M1C and V1C, respectively. Similar staining patterns were observed in macaques, with very little expression of *METTL7B* in corticocortical pyramidal neurons of neocortical and entorhinal layer 5A and upper layers (L2–L4). Using immunoelectron microscopy, we confirmed and extended previous reports, showing that *METTL7B* is localized to the ER and LDs in macaque and human hippocampal neurons and astrocytes (Figures 6H and 6I).

This preferential expression of *METTL7B* in humans and macaques prompted us to broaden our analysis and include in our study another primate, analyzing *METTL7B* in 16 homologous brain regions in humans, chimpanzees, and rhesus macaques (Sousa et al., 2017; Zhu et al., 2018). *METTL7B* expression in the chimpanzee brain was not distinct from that in humans, whereas it was upregulated more broadly throughout the cerebrum in the macaque brain (Figure S5E), which can possibly be attributed to the elevated expression in astrocytes (Figures 6A and S5B). Using published datasets (Cardoso-Moreira et al., 2019), we found that *METTL7B* expression was enriched in the human, chimpanzee, and macaque cerebrum but not in the cerebrum of the mouse, rat, rabbit, and opossum (Figure S5F), suggesting that the expression and its biological consequences are not conserved across mammals and likely are specific to primates.

METTL7B interacts with proteins associated with the ER, LDs, and AD

To gain more insights into the possible function of *METTL7B* in the primate hippocampus, we sought to identify *METTL7B*-interacting proteins by performing unbiased proteomics analysis with

(C) Rank of the hippocampus-specific genes based on their temporal specificity in the adult hippocampus using PsychENCODE data (Li et al., 2018). Top: coefficients of time group–region, with large positive values indicating upregulation along development (illustrated in the diagram). Bottom: differences in the time group–region coefficients between the HIP and the maxima of other regions.

(D) Integration of InNs from 4 regions. Gray dots denote cells from other regions.

(E) Expression of the exclusive markers (rows) of the cluster “InN *SST ADAMTS12*” across all InN subtypes (columns) in the HIP and EC and all *SST*⁺ InN subtypes (columns) in the MTG and dIPFC.

See also Figure S4.

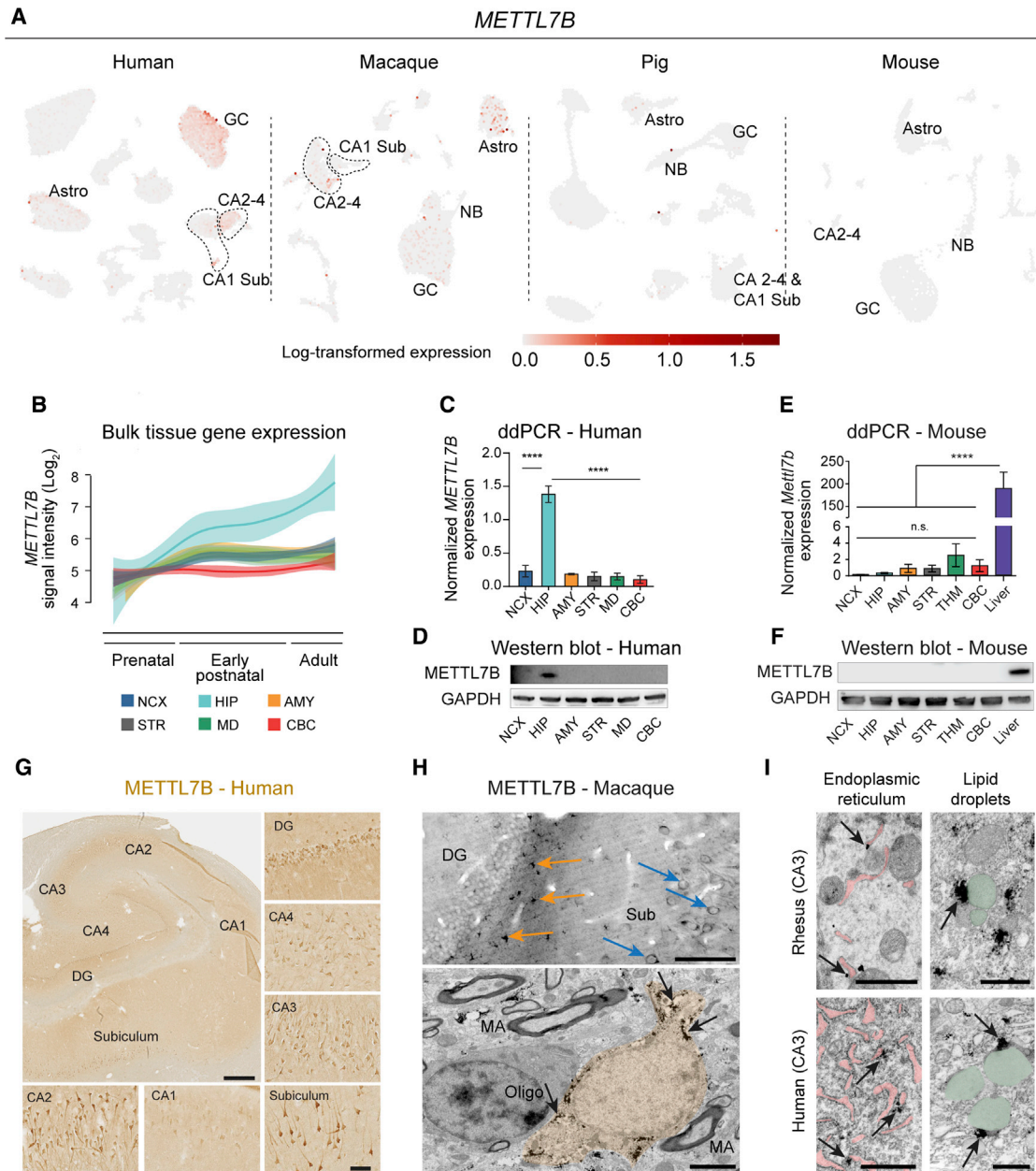


Figure 6. *METTL7B* defines subregion-specific ExNs and Astros in primates

(A) *METTL7B* expression in the adult human HIP-EC, macaque DG, pig HIP, and mouse DG.

(B) Expression of *METTL7B*, showing temporal specificity in the adult human hippocampus (Kang et al., 2011).

(C and D) Droplet digital PCR and immunoblot validation in six regions of the adult human brain. One-way ANOVA with post hoc Dunnett's adjustment (**** $p < 0.0001$), $n = 3$ per group.

(E and F) Same as (C) and (D) using mouse tissues, including liver as a positive control.

(G) *METTL7B* immunostaining of the adult human hippocampus. Scale bars: 1 mm; insets, 100 μm ; immunofluorescence, 10 μm .

(H) Top panel: numerous *METTL7B* immunopositive astrocytes (orange arrows) and neurons (blue arrows). Bottom panel: immunoelectron microscopy of Astros (orange; pointed with arrows). Scale bars, 100 μm (top) and 2 μm (bottom). MA, myelinated axon.

(I) Immunoelectron microscopy of CA3 hippocampal pyramidal neurons in rhesus macaque and human. Note *METTL7B* labeling (arrows) on the outer surface of ER cisterns (pink) and in contact with LDs (green). Scale bars, 1 μm .

All data are mean \pm SEM. **** $p < 0.0001$. See also Figure S5.

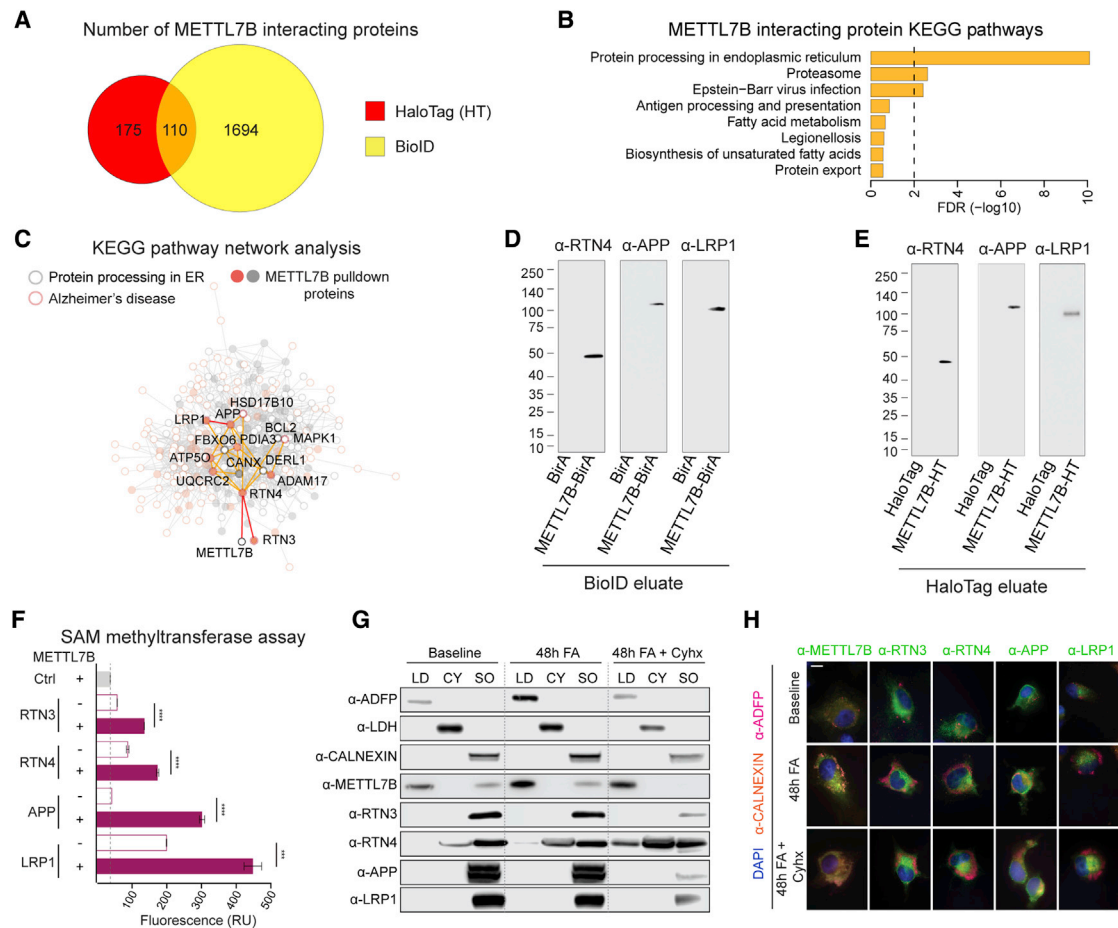


Figure 7. METTL7B-interacting proteins are enriched in the ER and LDs

(A) Venn diagram of high-confidence METTL7B-interacting proteins revealed by HaloTag and BioID.

(B) KEGG enrichment of METTL7B interacting proteins from the intersection of HaloTag and BioID.

(C) Interaction network with proteins in KEGG protein processing in the ER pathway (gray) and AD pathway (orange). METTL7B interactors are shown as filled circles.

(D and E) Immunoblot confirmation of top interacting candidates. The molecular weight of the RTN4-immunoreactive band is consistent with a known proteolytic fragment of RTN4A or RTN4B (Kim et al., 2003; Sekine et al., 2020).

(F) SAM methyltransferase activity assay showing increased reactivity in the presence of METTL7B. The p values were calculated by unpaired two-tailed Student's t test; n = 3.

(G and H) Immunoblot and immunofluorescence analysis of METTL7B translocation. An increased fatty acid (FA) load leads to a shift of METTL7B from the ER to lipid droplets (LDs), whereas high-confidence interactors remain unaffected. Blocking translation of new proteins with cycloheximide (Cyhx) suggests a complete shift of METTL7B. Scale bar, 10 μ m. CY, cytosol; SO, sedimented organelle (containing the ER).

All data are mean \pm SEM. ****p < 0.0001, ***p < 0.001. See also Figures S6 and S7 and Table S4.

two different affinity-based approaches: HaloTag, which has scarce non-specific binding (Hook, 2014), and BioID, which is able to capture weak or transient interactions (Roux et al., 2012; Figures S6A, S6B, S6G, and S6H). Using significance analysis of interactome (SAINT) (Choi et al., 2011), we identified 275 METTL7B interactors in HaloTag and 1,804 interactors in BioID (Figures S6D and S6J; Table S5; STAR Methods). Both methods showed significant enrichment in ER- and LD-associated proteins (Figures S6E and S6K), which was also confirmed by co-immunofluorescence (Figures S6C and S6I). KEGG pathway enrichment analysis revealed potential relevance to protein processing in the ER, oxidative phosphorylation, endocytosis,

and neurodegenerative diseases, including AD (Figures S6F and S6L).

Intersecting the lists of METTL7B-interacting proteins from both strategies, we found 110 high-confidence proteins, with the most enriched Gene Ontology term being protein processing in ER (Figures 7A and 7B). We observed that many of those high-confidence proteins overlapped with the KEGG AD pathway (Figures 7C and S6F), including amyloid precursor protein (APP), inhibition of γ -secretase (RTN3 and RTN4/NOGO), and amyloid binding (NAE1, LRP1, and APBB1). We confirmed, using our snRNA-seq dataset, that many of these genes were co-expressed extensively with *METTL7B* in several hippocampal

populations (Figure S7A), and subsequent immunoblotting confirmed that the candidate proteins RTN4, APP, and LRP1 were specific to METTL7B sample eluates. RTN3 was not detected in any of the samples, possibly because of low pull-down amounts (Figures 7D and 7E). Additionally, using multiple independent methods, including bulk tissue RNA-seq of multiple brain regions, snRNA-seq of the dlPFC (Mathys et al., 2019) and MTG (STAR Methods), and immunohistochemistry (Figures S7B–S7D), we found selective enrichment of METTL7B-expressing astrocytes in AD brains compared with control brains, suggesting that METTL7B expression may participate in the glial response to neuronal damage as AD progresses.

To determine whether the annotated methyltransferase domain of METTL7B exhibits methyltransferase activity, we incubated purified recombinant proteins (RTN4, APP, LRP1, and RTN3) with recombinant METTL7B in a continuous enzyme-coupled S-adenosylmethionine (SAM) methyltransferase assay. All four assayed samples produced a significant increase in signal compared with candidate proteins incubated alone (Figure 7F), suggesting that METTL7B uses SAM as a methyl donor and that METTL7B has enzymatic activity. We further showed that this METTL7B-mediated methylation could be limited under conditions with high levels of lipids because METTL7B was translocated from the ER to LDs in these conditions, but these METTL7B interacting proteins remained in the ER (Figures 7G and 7H). Our cross-species transcriptomics analysis suggests a region- and cell-type-specific protein methylation mechanism that seems to be restricted to primates.

DISCUSSION

We report an extensive single-cell transcriptomics analysis of several anatomically defined cell populations in the adult human, macaque, and pig hippocampal-entorhinal system. Our findings reveal fundamental species differences in adult hippocampal neurogenesis and delineate the molecular diversity of the cytoarchitectural transition from the allo- to the neocortex. These results also outline genes that are selectively enriched in certain species and cell types that may have a role in the specific biology and/or pathology of the hippocampal-entorhinal system

Unlike recent studies that mostly rely on one or two key markers (e.g., progenitors [nestin]; neuroblasts and immature granule cells [DCX]) (Boldrini et al., 2018; Moreno-Jiménez et al., 2019; Tobin et al., 2019), single-cell RNA-seq studies are more comprehensive because they leverage combinatorial gene expression profiles to identify cell populations more robustly (Hochgerner et al., 2018). This approach also allows cross-species analysis, amplifying rare signals within a single species that may be masked when analyzed separately. Our cross-species analysis allowed identification of the neurogenic lineage in the mouse, pig, and macaque, which was virtually absent in the human. We only detected one cell with the transcriptomics profile characteristic of nIPCs and one with putative neuroblast profile among 32,067 granule cells (0.003%) in our adult human DG samples, a proportion considerably lower than the expected 0.09%–3.8% neuroblasts according to previous DCX immunostaining or ¹⁴C incorporation studies of the adult human HIP (see Table S2 for data and relevant studies).

The same analytic strategy detected much higher proportions of neuroblasts in the other analyzed species (mouse, 6.6%; pig, 55.6%; macaque, 2.0%; Figure 2B; Table S3). These proportions were higher than those estimated previously based on progenitor proliferation and identification of neuroblasts markers such as DCX (Table S2), suggesting that more studies are needed to fine-tune detection of these neurogenic populations. However, this apparently lax detection protocol confirms that our parameters are unlikely to have missed any appreciable neuroblast populations among the large pool of surveyed human DG granule cells, even if they might exhibit an ambiguous profile.

Alternative confounding of our cross-species integrative analysis from possible human-specific transcriptomics changes was ruled out when human UMAP layouts did not include any clustering of neurogenic cells adjacent to the mature granule cell cluster. Likewise, the possibility that human neuroblasts exist in our samples but that their transcriptomics profile differs from other species and blends with related cell populations is lessened by findings that all neurogenic lineages preceding mature granule cells were absent in human DG samples (Tables S2 and S3).

We also extended our findings to existing snRNA-seq data of the adult human HIP. We reappraised the identity of a recently reported neural progenitor cluster (Ayhan et al., 2021) marked by *LPAR1*, a gene reported to mark mouse DG neural progenitors (Walker et al., 2016; Hochgerner et al., 2018). Our analyses indicated that this cluster actually represented doublets formed by oligodendrocytes and granule cells (Figure S3S). In addition, reanalysis of the pioneer HIP data (Habib et al., 2017) by Sorrells et al. (2021) showed that the cell cluster labeled as neural stem cells was actually characteristic of ependymal cells.

Analysis of *DCX* transcripts in all the analyzed species showed expression in mature neurons, mostly InNs, and in glial cells, indicating that *DCX* expression is not exclusive to DG neuroblasts (Figures 3A and 3B). This pattern is in agreement with the reanalysis of the data from Habib et al. (2017) (Sorrells et al., 2021). All transcriptomics analyses performed so far suggest a lack of neurogenic cell populations in the adult human DG.

At the protein level, DCX was, with a few exceptions (Figure S3L), present exclusively in DG cells resembling neuroblasts and immature granule cells in all analyzed non-human species. Also, cells with immature morphology could be detected in other areas, such as the EC of the macaque or the pyriform cortex of the mouse, as described previously (Gómez-Climent et al., 2008; Zhang et al., 2009). In humans, there is intense controversy regarding DCX immunostaining in the human DG, with some reports showing negative results (Dennis et al., 2016; Cipriani et al., 2018; Sorrells et al., 2018, 2021) and others describing DCX-IL cells (Knoth et al., 2010; Epp et al., 2013; Boldrini et al., 2018; Le Maître et al., 2018; Moreno-Jiménez et al., 2019, 2021; Tobin et al., 2019). We detected clear DCX-IL cells in the amygdala and occasionally in the EC, but we could not find DCX-IL cells resembling neuroblasts in the DG in the same tissue sections. These inconsistencies in detecting DCX-IL cells in the adult human DG cannot be fully attributed to postmortem denaturation and degradation of DCX protein because DCX-IL cells were clearly detected in samples with prolonged PMIs (Figures S3D, S3E, and S3I–S3L). Moreno-Jiménez et al. (2019) reported an intensive protocol for antigen retrieval as a necessary step to label

DCX cells in the human DG. However, they reported no positive cells in the EC, a relatively common finding in our study (Figure S3D) and another (Sorrells et al., 2021) using conventional antigen retrieval. Because our analysis did not reveal neuroblasts at the RNA or protein level (using diverse antigen retrieval methods), the question remains what those previously reported cells could be. Apart from underappreciated non-specific and off-target effects (Sorrells et al., 2021), those studies could label mature granule cells and InNs that might contain low levels of DCX protein that was detected specially after multi-step antigen retrieval. In support of this hypothesis is the fact that the faintly immunolabeled cells we detected mostly in the vicinity of the granule cell layer, exhibited the morphology of mature InNs, and some co-labeled with antibodies against GAD1, a marker of InNs (Figures 3E and S3M–S3Q). This faint staining is far from the strong staining and well-defined morphology of somata and dendrites revealed in the EC and in the amygdala (Figures S3D and S3E) and is similar to the light DCX immunostaining reported previously (Seki et al., 2019). Thus, our conclusion is that DCX protein might be expressed at very low levels in InNs or in some mature granule cells that can be lightly immunolabeled under normal antigen retrieval but can show more intense and widespread staining under more elaborate tissue treatment and stringent conditions of antigen retrieval. In fact, Figure 2I from Moreno-Jiménez et al. (2019) shows that around 75% of DCX-IL cells were colocalized with NeuN (RBFOX3, 75%), a marker of mature granule cells, and 91% of DCX-IL cells were also positive for Prospero homeobox1 (PROX1), a transcription factor expressed by granule cells that is also expressed by InNs generated in the caudal ganglionic eminence (Ma et al., 2013; Laclef and Métin, 2018), supporting the possibility that most DCX-IL cells might actually be mature granule cells or InNs.

Regarding RNA analysis, although the PMI for humans was longer than for other analyzed species, human brains were kept at 4°C for most of the PMI period, whereas the pigs used as controls for PMI were kept at room temperature. This warm PMI will likely exacerbate the postmortem effects, but those conditions were not an obstacle to detect the neurogenic pathway in this species. It could be argued that the neurogenic pathway in the human DG is not detected because our snRNA-seq strategy might preferentially exclude neurogenic cells in humans. However, it seems extremely unlikely that it will affect all cell types in the neurogenic lineage, from progenitors to neuroblasts, and only in human. Overall, the most parsimonious interpretation of the combined results from our RNA transcript analysis and the DCX protein study is that, contrary to the other analyzed mammals, ongoing baseline neurogenesis does not occur or is extremely rare in the adult human DG.

Similar species-related and cell-specific transcriptomics profiling that characterizes neurogenic potential also outlines the transition from allocortical to neocortical domains in the hippocampal-entorhinal system and shows that ExNs are the main drivers of the differences between subfields (Figure 4), which evidences a richer complement of ExNs than traditional descriptions based on cytoarchitecture. Our analysis provides a primer to further study these populations and characterize the possible implications for hippocampal-entorhinal physiology. These data refine our understanding of the evolution of the allo-, meso-, and

neocortex. The transcriptomics signatures we developed strongly suggest homology between the mammalian allocortex and specifically deep layers of the EC and neocortex.

Among the genes contributing to the layer transition, we identified METTL7B to be important in hippocampus physiology and function. We found that METTL7B, equipped with methyltransferase activity, interacts with important AD-related proteins (e.g., APP, LRP1, RTN3, and RTN4). Importantly, our results suggest that these functional interactions in a subset of ExNs and astrocytes seem to be phylogenetically specific to Old World monkeys and apes (parvorder Catarrhini), species that show more marked signs of pathology related to aging, such as AD, than other species (Perez et al., 2013; Finch and Austad, 2015; Edler et al., 2017; Paspalas et al., 2018). Overall, our analyses provide multiple vignettes of how this resource can be used to identify cell types and genes that might be functionally relevant for the biology of the hippocampus, allowing inter-species comparisons.

STAR★METHODS

Detailed methods are provided in the online version of this paper and include the following:

- KEY RESOURCES TABLE
- RESOURCE AVAILABILITY
 - Lead contact
 - Materials availability
 - Data and code availability
- EXPERIMENTAL MODEL AND SUBJECT DETAILS
 - Human, rhesus macaque and pig postmortem tissue
- METHOD DETAILS
 - Anatomical definition of sampled subregions of the hippocampal formation and entorhinal cortex
 - Brain cell nuclei isolation
 - Single nucleus microfluidic capture and cDNA synthesis
 - Single nucleus RNA-seq library preparation
 - Sequencing of libraries
 - Single nuclei expression quantification and quality control
 - Normalization, dimensionality reduction and clustering
 - Tree construction
 - Relative cell cluster contribution from subregions and donors
 - Global across-dataset comparison
 - Classification of cell subtypes in human
 - Classification of cell types in pig and rhesus macaque
 - Classification of cell types in fetal human hippocampus
 - Integrate dentate gyrus data across species and developmental stages
 - RNA velocity analysis for mouse, pig, rhesus macaque and human
 - Comparison of subtype markers across species and developmental stages
 - Expression profiling of *DCX* across species and regions
 - Enrichment of neurogenic marker sets in DCX-expressing cells

- Reanalysis of previous adult human hippocampus snRNA-seq data
- Cell subtype comparisons among HIP, EC, MTG and dIPFC
- Identifying genes specific to ExN of different regions
- Temporal specificity of the HIP ExN-specific genes in bulk tissue transcriptomic datasets
- Exclusive markers of cluster InN SST ADAMTS12
- Generation of knockout mice and tissue processing
- *In situ* hybridization
- Immunolabeling and histology
- IHC labeling for electron microscopy
- Plasmids
- Lentiviral purification and generation of stable cell lines
- Affinity capture of proteins
- Mass spectrometry and proteomic data analysis
- Protein identification and data analysis
- Identification of true pulldown proteins based on mass spectrometry spectral counting data
- Subcellular localization of METTL7B
- Validation of pulldown experiments
- KEGG pathway enrichment analysis
- Immunoblotting and silver stain
- SAM assay
- RNA isolation and digital droplet PCR
- snRNA-seq profiling of human Alzheimer's disease brain middle temporal gyrus
- **QUANTIFICATION AND STATISTICAL ANALYSIS**

SUPPLEMENTAL INFORMATION

Supplemental information can be found online at <https://doi.org/10.1016/j.neuron.2021.10.036>.

ACKNOWLEDGMENTS

We thank K. Meyer for help with gene expression analysis; A. Rosa Campos and K. Motamedchaboki (SBP Medical Discovery Institute, La Jolla, CA) for help with generating proteomics data; the University of Maryland Brain and Tissue Bank, M. Horn, M. Pletikos, and S. Wilson for assistance with tissue acquisition and processing; J. DeFelipe and the NIH NeuroBioBank for providing human tissue; and K. Gobeske and other lab colleagues for comments. We also thank A. Duque for using equipment from MacBrainResource (NIH/NIMH MH113257). This work was supported by NIH grants MH116488, MH124619, RF1AG074341, and DA023999. The project that gave rise to these results received the support of a fellowship from "la Caixa" Foundation (ID 100010434). The fellowship code is LCF/BQ/PI19/11690010. G. Santpere is supported by grant MS20/00064 from Instituto de Salud Carlos III (Spain) and cofunded by the European Social Fund and grant PID2019-104700GA-I00 funded by Agencia Estatal de Investigación, Spain.

AUTHOR CONTRIBUTIONS

D.F. and N.S. conceived and designed the study. D.F. and A.T.N.T. performed the METTL7B experiments. M.S. generated control snRNA-seq data. S.M., C.X., Q.L., G.S., M.L., and A.S. analyzed control snRNA-seq data. D.F., A.T.N.T., and H.T. performed immunostaining of AD tissue. J.I.A. performed DCX immunostaining. J.C. analyzed proteomics data. Y.M.M. performed immunoelectron microscopy. J.S., L.Z., and S.M.S. generated and analyzed AD snRNA-seq data. D.A., Z.V., A.H., S.Z., I.G., L.R., A.M.M.S., Y.L., and R.F. contributed to additional data collection. D.F., A.T.N.T., S.M., J.I.A., M.S., and N.S. wrote the manuscript. All authors edited the manuscript.

DECLARATION OF INTERESTS

The authors declare no competing interests.

Received: December 19, 2019

Revised: October 17, 2021

Accepted: October 26, 2021

Published: November 18, 2021

REFERENCES

- Abbott, L.C., and Nigussie, F. (2020). Adult neurogenesis in the mammalian dentate gyrus. *Anat. Histol. Embryol.* *49*, 3–16.
- Abul-Husn, N.S., Bushlin, I., Morón, J.A., Jenkins, S.L., Dolios, G., Wang, R., Iyengar, R., Ma'ayan, A., and Devi, L.A. (2009). Systems approach to explore components and interactions in the presynapse. *Proteomics* *9*, 3303–3315.
- Aibar, S., González-Blas, C.B., Moerman, T., Huynh-Thu, V.A., Imrichova, H., Hulselmans, G., Rambow, F., Marine, J.C., Geurts, P., Aerts, J., et al. (2017). SCENIC: single-cell regulatory network inference and clustering. *Nat. Methods* *14*, 1083–1086.
- Andersen, P. (2007). *The hippocampus book* (Oxford University Press).
- Angata, K., Suzuki, M., and Fukuda, M. (2002). ST8Sia II and ST8Sia IV polysialyltransferases exhibit marked differences in utilizing various acceptors containing oligosialic acid and short polysialic acid. The basis for cooperative polysialylation by two enzymes. *J. Biol. Chem.* *277*, 36808–36817.
- Arellano, J.I., Morozov, Y.M., Micali, N., and Rakic, P. (2021). Radial Glial Cells: New Views on Old Questions. *Neurochem. Res.* *46*, 2512–2524.
- Ayhan, F., Kulkarni, A., Berto, S., Sivaprakasam, K., Douglas, C., Lega, B.C., and Konopka, G. (2021). Resolving cellular and molecular diversity along the hippocampal anterior-to-posterior axis in humans. *Neuron* *109*, 2091–2105.e6.
- Becht, E., McInnes, L., Healy, J., Dutertre, C.A., Kwok, I.W.H., Ng, L.G., Ginhoux, F., and Newell, E.W. (2018). Dimensionality reduction for visualizing single-cell data using UMAP. *Nat. Biotechnol.* *37*, 38.
- Berg, D.A., Su, Y., Jimenez-Cyrus, D., Patel, A., Huang, N., Morizet, D., Lee, S., Shah, R., Ringeling, F.R., Jain, R., et al. (2019). A Common Embryonic Origin of Stem Cells Drives Developmental and Adult Neurogenesis. *Cell* *177*, 654–668.e15.
- Bergen, V., Lange, M., Peidli, S., Wolf, F.A., and Theis, F.J. (2020). Generalizing RNA velocity to transient cell states through dynamical modeling. *Nat. Biotechnol.* *38*, 1408–1414.
- Boldrini, M., Fulmore, C.A., Tartt, A.N., Simeon, L.R., Pavlova, I., Poposka, V., Rosoklija, G.B., Stankov, A., Arango, V., Dwork, A.J., et al. (2018). Human Hippocampal Neurogenesis Persists throughout Aging. *Cell Stem Cell* *22*, 589–599.e5.
- Bonaguidi, M.A., Wheeler, M.A., Shapiro, J.S., Stadel, R.P., Sun, G.J., Ming, G.L., and Song, H. (2011). In vivo clonal analysis reveals self-renewing and multipotent adult neural stem cell characteristics. *Cell* *145*, 1142–1155.
- Braak, H., and Del Tredici, K. (2015). Neuroanatomy and pathology of sporadic Alzheimer's disease. *Adv. Anat. Embryol. Cell Biol.* *215*, 1–162.
- Breunig, J.J., Sarkisian, M.R., Arellano, J.I., Morozov, Y.M., Ayoub, A.E., Sojitra, S., Wang, B., Flavell, R.A., Rakic, P., and Town, T. (2008). Primary cilia regulate hippocampal neurogenesis by mediating sonic hedgehog signaling. *Proc. Natl. Acad. Sci. USA* *105*, 13127–13132.
- Brill, L.M., Motamedchaboki, K., Wu, S., and Wolf, D.A. (2009). Comprehensive proteomic analysis of *Schizosaccharomyces pombe* by two-dimensional HPLC-tandem mass spectrometry. *Methods* *48*, 311–319.
- Butler, A., Hoffman, P., Smibert, P., Papalexis, E., and Satija, R. (2018). Integrating single-cell transcriptomic data across different conditions, technologies, and species. *Nat. Biotechnol.* *36*, 411–420.
- Buzsáki, G., and Moser, E.I. (2013). Memory, navigation and theta rhythm in the hippocampal-entorhinal system. *Nat. Neurosci.* *16*, 130–138.

- Cardoso-Moreira, M., Halbert, J., Valloton, D., Velten, B., Chen, C., Shao, Y., Liechti, A., Ascenção, K., Rummel, C., Ovchinnikova, S., et al. (2019). Gene expression across mammalian organ development. *Nature* 571, 505–509.
- Cembrowski, M.S., Bachman, J.L., Wang, L., Sugino, K., Shields, B.C., and Spruston, N. (2016a). Spatial Gene-Expression Gradients Underlie Prominent Heterogeneity of CA1 Pyramidal Neurons. *Neuron* 89, 351–368.
- Cembrowski, M.S., Wang, L., Sugino, K., Shields, B.C., and Spruston, N. (2016b). Hipposeq: a comprehensive RNA-seq database of gene expression in hippocampal principal neurons. *eLife* 5, e14997.
- Cembrowski, M.S., Phillips, M.G., DiLisio, S.F., Shields, B.C., Winnubst, J., Chandrashekar, J., Bas, E., and Spruston, N. (2018). Dissociable Structural and Functional Hippocampal Outputs via Distinct Subiculum Cell Classes. *Cell* 173, 1280–1292.e18.
- Centurion, L.A., and Swanson, L.W. (2007). Spatial organization of direct hippocampal field CA1 axonal projections to the rest of the cerebral cortex. *Brain Res. Brain Res. Rev.* 56, 1–26.
- Choi, H., Larsen, B., Lin, Z.Y., Breikreutz, A., Mellacheruvu, D., Fermin, D., Qin, Z.S., Tyers, M., Gingras, A.C., and Nesvizhskii, A.I. (2011). SAINT: probabilistic scoring of affinity purification-mass spectrometry data. *Nat. Methods* 8, 70–73.
- Cipriani, S., Nardelli, J., Verney, C., Delezoide, A.L., Guimiot, F., Gressens, P., and Adle-Biassette, H. (2016). Dynamic Expression Patterns of Progenitor and Pyramidal Neuron Layer Markers in the Developing Human Hippocampus. *Cereb. Cortex* 26, 1255–1271.
- Cipriani, S., Ferrer, I., Aronica, E., Kovacs, G.G., Verney, C., Nardelli, J., Khung, S., Delezoide, A.L., Milenkovic, I., Rasika, S., et al. (2018). Hippocampal Radial Glial Subtypes and Their Neurogenic Potential in Human Fetuses and Healthy and Alzheimer's Disease Adults. *Cereb. Cortex* 28, 2458–2478.
- Dennis, C.V., Suh, L.S., Rodriguez, M.L., Kril, J.J., and Sutherland, G.T. (2016). Human adult neurogenesis across the ages: An immunohistochemical study. *Neuropathol. Appl. Neurobiol.* 42, 621–638.
- Dobin, A., Davis, C.A., Schlesinger, F., Drenkow, J., Zaleski, C., Jha, S., Batut, P., Chaisson, M., and Gingeras, T.R. (2013). STAR: ultrafast universal RNA-seq aligner. *Bioinformatics* 29, 15–21.
- Dull, T., Zufferey, R., Kelly, M., Mandel, R.J., Nguyen, M., Trono, D., and Naldini, L. (1998). A third-generation lentivirus vector with a conditional packaging system. *J. Virol.* 72, 8463–8471.
- Edler, M.K., Sherwood, C.C., Meindl, R.S., Hopkins, W.D., Ely, J.J., Erwin, J.M., Mufson, E.J., Hof, P.R., and Raghanti, M.A. (2017). Aged chimpanzees exhibit pathologic hallmarks of Alzheimer's disease. *Neurobiol. Aging* 59, 107–120.
- Epp, J.R., Beasley, C.L., and Galea, L.A. (2013). Increased hippocampal neurogenesis and p21 expression in depression: dependent on antidepressants, sex, age, and antipsychotic exposure. *Neuropsychopharmacology* 38, 2297–2306.
- Eriksson, P.S., Perfilieva, E., Björk-Eriksson, T., Alborn, A.M., Nordborg, C., Peterson, D.A., and Gage, F.H. (1998). Neurogenesis in the adult human hippocampus. *Nat. Med.* 4, 1313–1317.
- Finch, C.E., and Austad, S.N. (2015). Commentary: is Alzheimer's disease uniquely human? *Neurobiol. Aging* 36, 553–555.
- Flor-García, M., Terreros-Roncal, J., Moreno-Jiménez, E.P., Ávila, J., Rábano, A., and Llorens-Martín, M. (2020). Unraveling human adult hippocampal neurogenesis. *Nat. Protoc.* 15, 668–693.
- Frazer, S., Prados, J., Niquille, M., Cadilhac, C., Markopoulos, F., Gomez, L., Tomasello, U., Telley, L., Holtmaat, A., Jabaudon, D., and Dayer, A. (2017). Transcriptomic and anatomic parcellation of 5-HT_{3AR} expressing cortical interneuron subtypes revealed by single-cell RNA sequencing. *Nat. Commun.* 8, 14219.
- Freund, T.F. (2002). Changes in the views of neuronal connectivity and communication after Cajal: examples from the hippocampus. *Prog. Brain Res.* 136, 203–213.
- Gloor, P. (1997). *The temporal lobe and limbic system* (Oxford University Press).
- Gómez-Climent, M.A., Castillo-Gómez, E., Varea, E., Guirado, R., Blasco-Ibáñez, J.M., Crespo, C., Martínez-Guijarro, F.J., and Nacher, J. (2008). A population of prenatally generated cells in the rat paleocortex maintains an immature neuronal phenotype into adulthood. *Cereb. Cortex* 18, 2229–2240.
- Gould, E., Tanapat, P., McEwen, B.S., Flugge, G., and Fuchs, E. (1998). Proliferation of granule cell precursors in the dentate gyrus of adult monkeys is diminished by stress. *Proc. Natl. Acad. Sci. USA* 95, 3168–3171.
- Grubman, A., Chew, G., Ouyang, J.F., Sun, G., Choo, X.Y., McLean, C., Simmons, R.K., Buckberry, S., Vargas-Landin, D.B., Poppe, D., et al. (2019). A single-cell atlas of entorhinal cortex from individuals with Alzheimer's disease reveals cell-type-specific gene expression regulation. *Nat. Neurosci.* 22, 2087–2097.
- Guidi, S., Bianchi, P., Alstrup, A.K., Henningsen, K., Smith, D.F., and Bartsch, R. (2011). Postnatal neurogenesis in the hippocampal dentate gyrus and subventricular zone of the Göttingen minipig. *Brain Res. Bull.* 85, 169–179.
- Habib, N., Avraham-Davidi, I., Basu, A., Burks, T., Shekhar, K., Hofree, M., Choudhury, S.R., Aguet, F., Gelfand, E., Ardlie, K., et al. (2017). Massively parallel single-nucleus RNA-seq with DroNc-seq. *Nat. Methods* 14, 955–958.
- Hochgerner, H., Zeisel, A., Lönnerberg, P., and Linnarsson, S. (2018). Conserved properties of dentate gyrus neurogenesis across postnatal development revealed by single-cell RNA sequencing. *Nat. Neurosci.* 21, 290–299.
- Hodge, R.D., Bakken, T.E., Miller, J.A., Smith, K.A., Barkan, E.R., Graybiel, L.T., Close, J.L., Long, B., Johansen, N., Penn, O., et al. (2019). Conserved cell types with divergent features in human versus mouse cortex. *Nature* 573, 61–68.
- Hodges, B.D., and Wu, C.C. (2010). Proteomic insights into an expanded cellular role for cytoplasmic lipid droplets. *J. Lipid Res.* 51, 262–273.
- Hoogland, P.V., and Vermeulen-Vanderzee, E. (1989). Efferent connections of the dorsal cortex of the lizard *Gekko gekko* studied with Phaseolus vulgaris-leucoagglutinin. *J. Comp. Neurol.* 285, 289–303.
- Hook, B. (2014). *Cleaner Protein with HaloTag Purification Resins*. https://www.promega.com/resources/pubhub/tpub_153-cleaner-protein-with-halotag-purification-resins-article/.
- Huang, W., Sherman, B.T., and Lempicki, R.A. (2009). Systematic and integrative analysis of large gene lists using DAVID bioinformatics resources. *Nat. Protoc.* 4, 44–57.
- Ishizuka, N. (2001). Laminar organization of the pyramidal cell layer of the subiculum in the rat. *J. Comp. Neurol.* 435, 89–110.
- Jabès, A., Lavenex, P.B., Amaral, D.G., and Lavenex, P. (2010). Quantitative analysis of postnatal neurogenesis and neuron number in the macaque monkey dentate gyrus. *Eur. J. Neurosci.* 31, 273–285.
- Kang, H.J., Kawasawa, Y.I., Cheng, F., Zhu, Y., Xu, X., Li, M., Sousa, A.M., Pletikos, M., Meyer, K.A., Sedmak, G., et al. (2011). Spatio-temporal transcriptome of the human brain. *Nature* 478, 483–489.
- Kempermann, G., Gage, F.H., Aigner, L., Song, H., Curtis, M.A., Thuret, S., Kuhn, H.G., Jessberger, S., Frankland, P.W., Cameron, H.A., et al. (2018). Human Adult Neurogenesis: Evidence and Remaining Questions. *Cell Stem Cell* 23, 25–30.
- Kim, J.E., Li, S., GrandPré, T., Qiu, D., and Strittmatter, S.M. (2003). Axon regeneration in young adult mice lacking Nogo-A/B. *Neuron* 38, 187–199.
- Kim, D.I., Kc, B., Zhu, W., Motamedchaboki, K., Doye, V., and Roux, K.J. (2014). Probing nuclear pore complex architecture with proximity-dependent biotinylation. *Proc. Natl. Acad. Sci. USA* 111, E2453–E2461.
- Klausberger, T., and Somogyi, P. (2008). Neuronal diversity and temporal dynamics: the unity of hippocampal circuit operations. *Science* 321, 53–57.
- Knoth, R., Singec, I., Ditter, M., Pantazis, G., Capetian, P., Meyer, R.P., Horvat, V., Volk, B., and Kempermann, G. (2010). Murine features of neurogenesis in the human hippocampus across the lifespan from 0 to 100 years. *PLoS ONE* 5, e8809.
- Kohler, S.J., Williams, N.I., Stanton, G.B., Cameron, J.L., and Greenough, W.T. (2011). Maturation time of new granule cells in the dentate gyrus of adult macaque monkeys exceeds six months. *Proc. Natl. Acad. Sci. USA* 108, 10326–10331.

- Kornack, D.R., and Rakic, P. (1999). Continuation of neurogenesis in the hippocampus of the adult macaque monkey. *Proc. Natl. Acad. Sci. USA* *96*, 5768–5773.
- Korsunsky, I., Millard, N., Fan, J., Slowikowski, K., Zhang, F., Wei, K., Baglaenko, Y., Brenner, M., Loh, P.R., and Raychaudhuri, S. (2019). Fast, sensitive and accurate integration of single-cell data with Harmony. *Nat. Methods* *16*, 1289–1296.
- Kostylev, M.A., Kaufman, A.C., Nygaard, H.B., Patel, P., Haas, L.T., Gunther, E.C., Vortmeyer, A., and Strittmatter, S.M. (2015). Prion-Protein-interacting Amyloid- β Oligomers of High Molecular Weight Are Tightly Correlated with Memory Impairment in Multiple Alzheimer Mouse Models. *J. Biol. Chem.* *290*, 17415–17438.
- Kostylev, M.A., Tuttle, M.D., Lee, S., Klein, L.E., Takahashi, H., Cox, T.O., Gunther, E.C., Zilm, K.W., and Strittmatter, S.M. (2018). Liquid and Hydrogel Phases of PrP^C Linked to Conformation Shifts and Triggered by Alzheimer's Amyloid- β Oligomers. *Mol. Cell* *72*, 426–443.e12.
- Kriegstein, A.R., and Connors, B.W. (1986). Cellular physiology of the turtle visual cortex: synaptic properties and intrinsic circuitry. *J. Neurosci.* *6*, 178–191.
- Kuhn, H.G., Toda, T., and Gage, F.H. (2018). Adult Hippocampal Neurogenesis: A Coming-of-Age Story. *J. Neurosci.* *38*, 10401–10410.
- La Manno, G., Soldatov, R., Zeisel, A., Braun, E., Hochgerner, H., Petukhov, V., Lidschreiber, K., Kastriti, M.E., Lönnerberg, P., Furlan, A., et al. (2018). RNA velocity of single cells. *Nature* *560*, 494–498.
- Laclef, C., and Métin, C. (2018). Conserved rules in embryonic development of cortical interneurons. *Semin. Cell Dev. Biol.* *76*, 86–100.
- Lanjakornsiripan, D., Pior, B.J., Kawaguchi, D., Furutachi, S., Tahara, T., Katsuyama, Y., Suzuki, Y., Fukazawa, Y., and Gotoh, Y. (2018). Layer-specific morphological and molecular differences in neocortical astrocytes and their dependence on neuronal layers. *Nat. Commun.* *9*, 1623.
- Le Maître, T.W., Dhanabalan, G., Bogdanovic, N., Alkass, K., and Druid, H. (2018). Effects of Alcohol Abuse on Proliferating Cells, Stem/Progenitor Cells, and Immature Neurons in the Adult Human Hippocampus. *Neuropsychopharmacology* *43*, 690–699.
- Lee, H., and Thuret, S. (2018). Adult Human Hippocampal Neurogenesis: Controversy and Evidence. *Trends Mol. Med.* *24*, 521–522.
- Leng, K., Li, E., Eser, R., Piergies, A., Sit, R., Tan, M., Neff, N., Li, S.H., Rodriguez, R.D., Suemoto, C.K., et al. (2021). Molecular characterization of selectively vulnerable neurons in Alzheimer's disease. *Nat. Neurosci.* *24*, 276–287.
- Li, M., Santpere, G., Imamura Kawasawa, Y., Evgrafov, O.V., Gulden, F.O., Pochareddy, S., Sunkin, S.M., Li, Z., Shin, Y., Zhu, Y., et al.; BrainSpan Consortium; PsychENCODE Consortium; PsychENCODE Developmental Subgroup (2018). Integrative functional genomic analysis of human brain development and neuropsychiatric risks. *Science* *362*, eaat7615.
- Lois, C., Hong, E.J., Pease, S., Brown, E.J., and Baltimore, D. (2002). Germine transmission and tissue-specific expression of transgenes delivered by lentiviral vectors. *Science* *295*, 868–872.
- Luzzati, F. (2015). A hypothesis for the evolution of the upper layers of the neocortex through co-option of the olfactory cortex developmental program. *Front. Neurosci.* *9*, 162.
- Ma, T., Wang, C., Wang, L., Zhou, X., Tian, M., Zhang, Q., Zhang, Y., Li, J., Liu, Z., Cai, Y., et al. (2013). Subcortical origins of human and monkey neocortical interneurons. *Nat. Neurosci.* *16*, 1588–1597.
- Mathys, H., Davila-Velderrain, J., Peng, Z., Gao, F., Mohammadi, S., Young, J.Z., Menon, M., He, L., Abdurrob, F., Jiang, X., et al. (2019). Single-cell transcriptomic analysis of Alzheimer's disease. *Nature* *570*, 332–337.
- Matsuda, T., and Cepko, C.L. (2004). Electroporation and RNA interference in the rodent retina in vivo and in vitro. *Proc. Natl. Acad. Sci. USA* *101*, 16–22.
- Mercer, A., and Thomson, A.M. (2017). Cornu Ammonis Regions-Antecedents of Cortical Layers? *Front. Neuroanat.* *11*, 83.
- Mikkonen, M., Soininen, H., Kälviäinen, R., Tapiola, T., Ylilinen, A., Vapalahti, M., Paljärvi, L., and Pitkänen, A. (1998). Remodeling of neuronal circuitries in human temporal lobe epilepsy: increased expression of highly polysialylated neural cell adhesion molecule in the hippocampus and the entorhinal cortex. *Ann. Neurol.* *44*, 923–934.
- Moreno-Jiménez, E.P., Flor-García, M., Terreros-Roncal, J., Rábano, A., Cafini, F., Pallas-Bazarra, N., Ávila, J., and Llorens-Martín, M. (2019). Adult hippocampal neurogenesis is abundant in neurologically healthy subjects and drops sharply in patients with Alzheimer's disease. *Nat. Med.* *25*, 554–560.
- Moreno-Jiménez, E.P., Terreros-Roncal, J., Flor-García, M., Rábano, A., and Llorens-Martín, M. (2021). Evidences for Adult Hippocampal Neurogenesis in Humans. *J. Neurosci.* *41*, 2541–2553.
- Nesvizhskii, A.I., Keller, A., Kolker, E., and Aebersold, R. (2003). A statistical model for identifying proteins by tandem mass spectrometry. *Anal. Chem.* *75*, 4646–4658.
- Ngwenya, L.B., Peters, A., and Rosene, D.L. (2006). Maturational sequence of newly generated neurons in the dentate gyrus of the young adult rhesus monkey. *J. Comp. Neurol.* *498*, 204–216.
- Nielsen, J.V., Blom, J.B., Norberg, J., and Jensen, N.A. (2010). Zbtb20-induced CA1 pyramidal neuron development and area enlargement in the cerebral midline cortex of mice. *Cereb. Cortex* *20*, 1904–1914.
- Oberheim, N.A., Takano, T., Han, X., He, W., Lin, J.H., Wang, F., Xu, Q., Wyatt, J.D., Pilcher, W., Ojemann, J.G., et al. (2009). Uniquely hominid features of adult human astrocytes. *J. Neurosci.* *29*, 3276–3287.
- Ohara, S., Onodera, M., Simonsen, O.W., Yoshino, R., Hioki, H., Iijima, T., Tsutsui, K.I., and Witter, M.P. (2018). Intrinsic Projections of Layer Vb Neurons to Layers Va, III, and II in the Lateral and Medial Entorhinal Cortex of the Rat. *Cell Rep.* *24*, 107–116.
- Paredes, M.F., Sorrells, S.F., Cebrian-Silla, A., Sandoval, K., Qi, D., Kelley, K.W., James, D., Mayer, S., Chang, J., Auguste, K.I., et al. (2018). Does Adult Neurogenesis Persist in the Human Hippocampus? *Cell Stem Cell* *23*, 780–781.
- Park, S.K., Venable, J.D., Xu, T., and Yates, J.R., 3rd (2008). A quantitative analysis software tool for mass spectrometry-based proteomics. *Nat. Methods* *5*, 319–322.
- Park, S.M., Jang, H.J., and Lee, J.H. (2019). Roles of Primary Cilia in the Developing Brain. *Front. Cell. Neurosci.* *13*, 218.
- Paspalas, C.D., Carlyle, B.C., Leslie, S., Preuss, T.M., Crimins, J.L., Huttner, A.J., van Dyck, C.H., Rosene, D.L., Nairn, A.C., and Arnsten, A.F.T. (2018). The aged rhesus macaque manifests Braak stage III/IV Alzheimer's-like pathology. *Alzheimers Dement.* *14*, 680–691.
- Patzke, N., Spocter, M.A., Karlsson, K.A.E., Bertelsen, M.F., Haagensen, M., Chawana, R., Streicher, S., Kaswera, C., Gilissen, E., Alagaili, A.N., et al. (2015). In contrast to many other mammals, cetaceans have relatively small hippocampi that appear to lack adult neurogenesis. *Brain Struct. Funct.* *220*, 361–383.
- Perez, S.E., Raghanti, M.A., Hof, P.R., Kramer, L., Ikonovic, M.D., Lacor, P.N., Erwin, J.M., Sherwood, C.C., and Mufson, E.J. (2013). Alzheimer's disease pathology in the neocortex and hippocampus of the western lowland gorilla (*Gorilla gorilla gorilla*). *J. Comp. Neurol.* *527*, 4318–4338.
- Ramsden, H.L., Sürmeli, G., McDonagh, S.G., and Nolan, M.F. (2015). Laminar and dorsoventral molecular organization of the medial entorhinal cortex revealed by large-scale anatomical analysis of gene expression. *PLoS Comput. Biol.* *11*, e1004032.
- Reiner, A. (1991). A comparison of neurotransmitter-specific and neuropeptide-specific neuronal cell types present in the dorsal cortex in turtles with those present in the isocortex in mammals: implications for the evolution of isocortex. *Brain Behav. Evol.* *38*, 53–91.
- Rhee, S., Kirschen, G.W., Gu, Y., and Ge, S. (2016). Depletion of primary cilia from mature dentate granule cells impairs hippocampus-dependent contextual memory. *Sci. Rep.* *6*, 34370.
- Robinson, P.N., Wollstein, A., Böhme, U., and Beattie, B. (2004). Ontologizing gene-expression microarray data: characterizing clusters with Gene Ontology. *Bioinformatics* *20*, 979–981.

- Roux, K.J., Kim, D.I., Raida, M., and Burke, B. (2012). A promiscuous biotin ligase fusion protein identifies proximal and interacting proteins in mammalian cells. *J. Cell Biol.* *196*, 801–810.
- Roux, K.J., Kim, D.I., and Burke, B. (2013). BioID: a screen for protein-protein interactions. *Curr. Protoc. Protein Sci.* *74*, 19.23.1–19.23.15.
- Schmidt-Kastner, R., and Freund, T.F. (1991). Selective vulnerability of the hippocampus in brain ischemia. *Neuroscience* *40*, 599–636.
- Seki, T. (2002). Expression patterns of immature neuronal markers PSA-NCAM, CRMP-4 and NeuroD in the hippocampus of young adult and aged rodents. *J. Neurosci. Res.* *70*, 327–334.
- Seki, T., Hori, T., Miyata, H., Maehara, M., and Namba, T. (2019). Analysis of proliferating neuronal progenitors and immature neurons in the human hippocampus surgically removed from control and epileptic patients. *Sci. Rep.* *9*, 18194.
- Sekine, Y., Lindborg, J.A., and Strittmatter, S.M. (2020). A proteolytic C-terminal fragment of Nogo-A (reticulon-4A) is released in exosomes and potently inhibits axon regeneration. *J. Biol. Chem.* *295*, 2175–2183.
- Shepherd, G.M., and Rowe, T.B. (2017). Neocortical Lamination: Insights from Neuron Types and Evolutionary Precursors. *Front. Neuroanat.* *11*, 100.
- Slomianka, L., Amrein, I., Knuesel, I., Sørensen, J.C., and Wolfner, D.P. (2011). Hippocampal pyramidal cells: the reemergence of cortical lamination. *Brain Struct. Funct.* *216*, 301–317.
- Smyth, G.K., Michaud, J., and Scott, H.S. (2005). Use of within-array replicate spots for assessing differential expression in microarray experiments. *Bioinformatics* *21*, 2067–2075.
- Sorrells, S.F., Paredes, M.F., Cebrian-Silla, A., Sandoval, K., Qi, D., Kelley, K.W., James, D., Mayer, S., Chang, J., Auguste, K.I., et al. (2018). Human hippocampal neurogenesis drops sharply in children to undetectable levels in adults. *Nature* *555*, 377–381.
- Sorrells, S.F., Paredes, M.F., Velmeshev, D., Herranz-Pérez, V., Sandoval, K., Mayer, S., Chang, E.F., Insausti, R., Kriegstein, A.R., Rubenstein, J.L., et al. (2019). Immature excitatory neurons develop during adolescence in the human amygdala. *Nat. Commun.* *10*, 2748.
- Sorrells, S.F., Paredes, M.F., Zhang, Z., Kang, G., Pastor-Alonso, O., Biagiotti, S., Page, C.E., Sandoval, K., Knox, A., Connolly, A., et al. (2021). Positive Controls in Adults and Children Support That Very Few, If Any, New Neurons Are Born in the Adult Human Hippocampus. *J. Neurosci.* *41*, 2554–2565.
- Sousa, A.M.M., Zhu, Y., Raghanti, M.A., Kitchen, R.R., Onorati, M., Tebbenkamp, A.T.N., Stutz, B., Meyer, K.A., Li, M., Kawasawa, Y.I., et al. (2017). Molecular and cellular reorganization of neural circuits in the human lineage. *Science* *358*, 1027–1032.
- Spalding, K.L., Bergmann, O., Alkass, K., Bernard, S., Salehpour, M., Huttner, H.B., Boström, E., Westerlund, I., Vial, C., Buchholz, B.A., et al. (2013). Dynamics of hippocampal neurogenesis in adult humans. *Cell* *153*, 1219–1227.
- Stark, C., Breitkreutz, B.J., Reguly, T., Boucher, L., Breitkreutz, A., and Tyers, M. (2006). BioGRID: a general repository for interaction datasets. *Nucleic Acids Res.* *34*, D535–D539.
- Stuart, T., Butler, A., Hoffman, P., Hafemeister, C., Papalexi, E., Mauck, W.M., 3rd, Hao, Y., Stoeckius, M., Smibert, P., and Satija, R. (2019). Comprehensive Integration of Single-Cell Data. *Cell* *177*, 1888–1902.e21.
- Suzuki, W.A., and Amaral, D.G. (2004). Functional neuroanatomy of the medial temporal lobe memory system. *Cortex* *40*, 220–222.
- Tabb, D.L., McDonald, W.H., and Yates, J.R., 3rd (2002). DTASelect and Contrast: tools for assembling and comparing protein identifications from shotgun proteomics. *J. Proteome Res.* *1*, 21–26.
- Tang, Q., Ebbesen, C.L., Sanguinetti-Scheck, J.I., Preston-Ferrer, P., Gundlfinger, A., Winterer, J., Beed, P., Ray, S., Naumann, R., Schmitz, D., et al. (2015). Anatomical Organization and Spatiotemporal Firing Patterns of Layer 3 Neurons in the Rat Medial Entorhinal Cortex. *J. Neurosci.* *35*, 12346–12354.
- Tasic, B., Yao, Z., Graybiel, L.T., Smith, K.A., Nguyen, T.N., Bertagnolli, D., Goldy, J., Garren, E., Economo, M.N., Viswanathan, S., et al. (2018). Shared and distinct transcriptomic cell types across neocortical areas. *Nature* *563*, 72–78.
- Teo, G., Liu, G., Zhang, J., Nesvizhskii, A.I., Gingras, A.C., and Choi, H. (2014). SAINTexpress: improvements and additional features in Significance Analysis of INteractome software. *J. Proteomics* *100*, 37–43.
- Thomas, A., Klein, M.S., Stevens, A.P., Reinders, Y., Hellerbrand, C., Dettmer, K., Gronwald, W., Oefner, P.J., and Reinders, J. (2013). Changes in the hepatic mitochondrial and membrane proteome in mice fed a non-alcoholic steatohepatitis inducing diet. *J. Proteomics* *80*, 107–122.
- Tobin, M.K., Musaraca, K., Disouky, A., Shetti, A., Bheri, A., Honer, W.G., Kim, N., Dawe, R.J., Bennett, D.A., Arfanakis, K., and Lazarov, O. (2019). Human Hippocampal Neurogenesis Persists in Aged Adults and Alzheimer's Disease Patients. *Cell Stem Cell* *24*, 974–982.e3.
- Turró, S., Ingelmo-Torres, M., Estanyol, J.M., Tebar, F., Fernández, M.A., Albor, C.V., Gaus, K., Grewal, T., Enrich, C., and Pol, A. (2006). Identification and characterization of associated with lipid droplet protein 1: A novel membrane-associated protein that resides on hepatic lipid droplets. *Traffic* *7*, 1254–1269.
- Uhlén, M., Fagerberg, L., Hallström, B.M., Lindskog, C., Oksvold, P., Mardinoglu, A., Sivertsson, Å., Kampf, C., Sjöstedt, E., Asplund, A., et al. (2015). Proteomics. Tissue-based map of the human proteome. *Science* *347*, 1260419.
- Vanlandewijck, M., He, L., Mäe, M.A., Andrae, J., Ando, K., Del Gaudio, F., Nahar, K., Lebouvier, T., Laviña, B., Gouveia, L., et al. (2018). A molecular atlas of cell types and zonation in the brain vasculature. *Nature* *554*, 475–480.
- Velmeshev, D., Schirmer, L., Jung, D., Haeussler, M., Perez, Y., Mayer, S., Bhaduri, A., Goyal, N., Rowitch, D.H., and Kriegstein, A.R. (2019). Single-cell genomics identifies cell type-specific molecular changes in autism. *Science* *364*, 685–689.
- Walker, T.L., Overall, R.W., Vogler, S., Sykes, A.M., Ruhwald, S., Lasse, D., Ichwan, M., Fabel, K., and Kempermann, G. (2016). Lysophosphatidic Acid Receptor Is a Functional Marker of Adult Hippocampal Precursor Cells. *Stem Cell Reports* *6*, 552–565.
- Witter, M.P., Doan, T.P., Jacobsen, B., Nilssen, E.S., and Ohara, S. (2017). Architecture of the Entorhinal Cortex A Review of Entorhinal Anatomy in Rodents with Some Comparative Notes. *Front. Syst. Neurosci.* *11*, 46.
- Wolock, S.L., Lopez, R., and Klein, A.M. (2019). Scrublet: Computational Identification of Cell Doublets in Single-Cell Transcriptomic Data. *Cell Syst.* *8*, 281–291.e9.
- Xu, T., Venable, J.D., Park, S.K., Cociorva, D., Lu, B., Liao, L., Wohlschlegel, J., Hewel, J., and Yates, J.R. (2006). ProLuCID, a fast and sensitive tandem mass spectra-based protein identification program. *Mol. Cell. Proteomics* *5*, S174.
- Yao, Z., van Velthoven, C.T.J., Nguyen, T.N., Goldy, J., Sedeno-Cortes, A.E., Baftizadeh, F., Bertagnolli, D., Casper, T., Chiang, M., Crichton, K., et al. (2021). A taxonomy of transcriptomic cell types across the isocortex and hippocampal formation. *Cell* *184*, 3222–3241.e26.
- Yuan, T.F., Li, J., Ding, F., and Arias-Carrion, O. (2014). Evidence of adult neurogenesis in non-human primates and human. *Cell Tissue Res.* *358*, 17–23.
- Zeisel, A., Muñoz-Manchado, A.B., Codeluppi, S., Lönnerberg, P., La Manno, G., Juréus, A., Marques, S., Munguba, H., He, L., Betsholtz, C., et al. (2015). Brain structure. Cell types in the mouse cortex and hippocampus revealed by single-cell RNA-seq. *Science* *347*, 1138–1142.
- Zhang, X.M., Cai, Y., Chu, Y., Chen, E.Y., Feng, J.C., Luo, X.G., Xiong, K., Struble, R.G., Clough, R.W., Patrylo, P.R., et al. (2009). Doublecortin-expressing cells persist in the associative cerebral cortex and amygdala in aged nonhuman primates. *Front. Neuroanat.* *3*, 17.
- Zhong, S., Ding, W., Sun, L., Lu, Y., Dong, H., Fan, X., Liu, Z., Chen, R., Zhang, S., Ma, Q., et al. (2020). Decoding the development of the human hippocampus. *Nature* *577*, 531–536.
- Zhu, Y., Sousa, A.M.M., Gao, T., Skarica, M., Li, M., Santpere, G., Esteller-Cucala, P., Juan, D., Ferrández-Peral, L., Gulden, F.O., et al. (2018). Spatiotemporal transcriptomic divergence across human and macaque brain development. *Science* *362*, eaat8077.

STAR★METHODS

KEY RESOURCES TABLE

REAGENT or RESOURCE	SOURCE	IDENTIFIER
Antibodies		
a-Streptavidin-Cy3 (1:1000)	BioLegend	Cat#405215
a-Streptavidin-HRP, high sensitivity (1:40,000)	Pierce	Cat#21130
Chicken a-ADFP (1:1000)	Abcam	Cat#ab37516; RRID:AB_722641
Chicken a-BirA (1:1000)	Abcam	Cat#ab14002; RRID:AB_300830
Donkey a-Goat	Jackson ImmunoResearch	Cat#705-225-147; RRID:AB_2307341
Donkey a-Guinea pig IgG (H+L), biotin	Jackson ImmunoResearch	Cat#706-065-148; RRID:AB_2340451
Donkey a-Mouse, Alexa Fluor 555	Invitrogen	Cat#A-31570; RRID:AB_2536180
Donkey a-Rabbit IgG (H+L), biotin	Jackson ImmunoResearch	Cat#711-065-152; RRID:AB_2340593
Donkey a-Rabbit IgG, Alexa Fluor 488	Invitrogen	Cat#A-21206; RRID:AB_2535792
Donkey streptavidin conjugated	Jackson ImmunoResearch	Cat#016-160-084; RRID:AB_2337244
Goat a-Chicken IgY H&L (HRP)	Abcam	Cat#ab97150 RRID:AB_10679811
Goat a-Chicken IgY, Alexa Fluor 647	Invitrogen	Cat#A-21449; RRID:AB_2535866
Goat a-GAD1 (1:200)	R&D	Cat#AF2086; RRID:AB_2107724
Goat a-Rabbit IgG H&L (HRP)	Abcam	Cat#ab97080; RRID:AB_10679808
Guinea pig a-DCX (1:4000)	EMD Millipore	Cat#AB2253; RRID:AB_1586992
Mouse a-DCX (1:500)	Santa Cruz	Cat#sc-271390; RRID:AB_10610966
Mouse a-PSA-NCAM (1:500)	DBSH	Cat#5A5 s; RRID:AB_528392
Mouse a-CALNEXIN (1:50)	Santa Cruz	Cat#sc-23954; RRID:AB_626783
Mouse a-GAPDH (1:2500)	Invitrogen	Cat#MA5-15738-HRP; RRID:AB_2537659
Mouse a-HaloTag (1:1000)	Promega	Cat#G9211; RRID:AB_2688011
Rabbit a-APP (Y188) (1:200 IF, 1:10,000 WB)	Abcam	Cat#ab32136; RRID:AB_2289606
Rabbit a-b-galactosidase (1:500)	Invitrogen	Cat#A-11132; RRID:AB_22153
Rabbit a-CALNEXIN (1:1000)	Cell Signaling	Cat#2679; RRID:AB_2228381
Rabbit a-Lactate Dehydrogenase (1:5000)	Abcam	Cat#ab52488; RRID:AB_2134961
Rabbit a-LRP1 (1:200 IF, 1:1000 WB)	Abcam	Cat#ab92544; RRID:AB_2234877
Rabbit a-METTL7B (1:500 IHC, 1:1000 WB)	Atlas Antibodies	Cat#HPA038644; RRID:AB_2676130
Rabbit a-RTN3 (1:50 IF, 1:1000 WB)	Protein Tech	Cat# 12055-2-AP; RRID:AB_2301357
Rabbit a-RTN4 (NOGO A+B) (1:200 IF, 1:2000 WB)	Abcam	Cat#ab47085; RRID:AB_881718
Vectastain ABC-AP kit	Vector Labs	Cat#AK-5000;RRID:AB_2336792
Vector Blue AP kit	Vector Labs	Cat#SL-5300
Vectastain Elite ABC-HRP kit	Vector Labs	Cat#PK-6100;RRID:AB_2336819
CFWS Gelatin	Aurion	Cat#900.033
ImmPRES Excel Amplified HRP Polymer Staining Kit	Vector Labs	Cat#MP-7601-15
R-Gent SE-LM	Aurion	Cat#500.011
Goat-anti-Rabbit IgG (H&L) (gold particles conjugated)	Aurion	Cat#806.011;RRID:AB_2732799
Durcupan ACM	Sigma	Cat#44610
Anti-Digoxigenin-AP, Fab fragments	Roche	Cat#11093274910;RRID:AB_514497
Chemicals, peptides, and recombinant proteins		
APP (peptide)	rPeptide	Cat#A-1203-1
LRP1	Abnova	Cat#H00004035-G01

(Continued on next page)

Continued

REAGENT or RESOURCE	SOURCE	IDENTIFIER
METTL7B (24-244 aa)	GenScript	This paper
RTN3	Antibodies-Online	Cat#ABIN3111137
RTN4	Sino Biological	Cat#13030-H09E
Digoxigenin-UTP	Roche	Cat#11209256910
BsrGI	New England BioLabs	Cat#R0575L
Pacl	New England BioLabs	Cat#R0547L
Klenow	New England BioLabs	Cat#M0210M
Trypsin Gold, Mass Spectrometry Grade	Promega	Cat#V5280
PolyJet	SignaGen	Cat#SL100688
Protamine sulfate	MP Biomedicals	Cat#02194729
NBT/BCIP Stock Solution	Roche	Cat# 11681451001
Protector RNase Inhibitor	Roche	Cat#03335402001
cOmplete, EDTA-free Protease Inhibitor Cocktail	Roche	Cat#11836170001
Optiprep	Axis-Shield	Cat#1114542
Bovine Serum Albumin (BSA), Fraction V—Molecular Biology Grade	Gemini Bio-Products	Cat#700-106P
Critical commercial assays		
Chromium Single Cell 3' GEM, Library & Gel Bead Kit v3	10x Genomics	Cat#PN-1000075
TMRDirect (1:1000)	Promega	Cat#G2991
HaloTag	Promega	Cat#G6500
C18 TopTip	PolyLC	Cat#TT10C18.96
Chromium Single Cell B Chip Kit	10x Genomics	Cat#PN-1000074
Chromium i7 Multiplex Kit (10x Genomics #PN-120262)	10x Genomics	Cat#PN-120262
Deposited data		
Human adult hippocampus snRNA-seq	This paper	GSE186538
GRCh38 (Ensembl release 98)	Ensembl, GENCODE	https://www.encodegenes.org/human/#
Mmul10	UCSC, RefSeq	https://hgdownload.soe.ucsc.edu/goldenPath/rheMac10/bigZips/
susScr11	UCSC, RefSeq	https://hgdownload.soe.ucsc.edu/goldenPath/susScr11/bigZips/
PsychENCODE RNA-seq data	Li et al., 2018	http://www.development.psychencode.org/
Developmental human brain exon array data	Kang et al., 2011	https://hbatlas.org/
Human, chimpanzee and macaque RNA-seq data	Zhu et al., 2018	https://evolution.psychencode.org/
Mammalian brain development RNA-seq data	Cardoso-Moreira et al., 2019	https://apps.kaessmannlab.org/evodevoapp/
Human fetal hippocampus scRNA-seq data	Zhong et al., 2020	GSE131258
Mouse adult hippocampus scRNA-seq data	Hochgerner et al., 2018	GSE95753
Human hippocampus DroNc-seq data	Habib et al., 2017	https://singlecell.broadinstitute.org/single_cell
Axis-specific human hippocampus snRNA-seq data	Ayhan et al., 2021	https://cells.ucsc.edu/?ds=human-hippo-axis
snRNA-seq data of human Alzheimer's disease brain middle temporal gyrus	NCBI GEO	GSE188545

(Continued on next page)

Continued

REAGENT or RESOURCE	SOURCE	IDENTIFIER
snRNA-seq data of human Alzheimer's disease brain prefrontal cortex	Mathys et al., 2019	https://www.synapse.org/#!/Synapse:syn18485175
Bulk tissue RNA-seq data of Alzheimer's disease brains	Swarup Lab	https://swaruplab.bio.uci.edu/bulkRNA/
Experimental models: Cell lines		
Targeted embryonic stem (ES) cells Mettl7b ^{tm1(KOMP)Vlcg}	Knockout Mouse Project (KOMP) repository	https://www.komp.org/redirect.html
ReN-CAG-BirA	This paper	N/A
ReN-CAG-METTL7B-BirA	This paper	N/A
ReN-CAG-HaloTag	This paper	N/A
ReN-CAG-METTL7B-HaloTag	This paper	N/A
Lenti-X 293T cells	Clontech	Cat#632180
ReNcell CX	EMD Millipore	Cat#SCC007 RRID:CVCL_E922
Experimental models: Organisms/strains		
Mettl7b ^{tm1(KOMP)Vlcg} Chimeric Mice	Yale Genome Editing Center	https://medicine.yale.edu/compmed/ags/
Oligonucleotides		
Primers for genotyping Mettl7b ^{tm1(KOMP)Vlcg} Chimeric Mice	This paper	See Table S6
asMTfwd 5'-ATGGACATCCTGGTCC CACT-3'	This paper	See Table S6
asMTrev 5'-GCAATTAATACGACTC ACTAT AGGGAGATTTGACAGCCTTTCCCAT GATGT-3'	This paper	See Table S6
Human METTL7B IDT (Hs.Pt.58.39517850)	This paper	See Table S6
Human TBP IDT (Hs.PT.58v.39858774)	This paper	See Table S6
Mouse Mettl7b-fwd 5'-GGTCAGGTAAGCATGAGAGAG-3'	This paper	See Table S6
Mouse Mettl7b-probe 5'-/56-FAM/CGTGCAG/ZEN/GGTGAT CATT CAT CA/3IABkFQ/-3'	This paper	See Table S6
Recombinant DNA		
METTL7B, cDNA (NM_152637.2)	This paper	Integrated DNA Technologies
pHTC-CMV/neo-HaloTag	Promega	Cat#G7711
pMD2.G	Dull et al., 1998	Addgene #12259
pRSVrev	Dull et al., 1998	Addgene #12253
pMDLg/pRRE	Dull et al., 1998	Addgene #12251
pDTET-METTL7B	This paper	N/A
hPKG promoter (M60581.1)	This paper	Integrated DNA Technologies
pCAGIG	Matsuda and Cepko, 2004	Addgene #11159
pFUGW	Lois et al., 2002	Addgene #14883
pcDNA3.1-MCS-BirA(R118G)-HA	Roux et al., 2012	Addgene #36047
pCW57.1	David Root	Addgene #41393
Software and algorithms		
Cell Ranger v3.0.2	10x Genomics	https://support.10xgenomics.com/single-cell-gene-expression/software/downloads/latest
R version 3.6.1	R project	https://www.r-project.org/
Seurat v3	Stuart et al., 2019	https://satijalab.org/seurat/index.html
Harmony	Korsunsky et al., 2019	https://github.com/immunogenomics/harmony

(Continued on next page)

Continued		
REAGENT or RESOURCE	SOURCE	IDENTIFIER
scrublet	Wolock et al., 2019	https://github.com/swolock/scrublet
AUCell	Aibar et al., 2017	https://github.com/aertslab/AUCell
UMAP	Becht et al., 2018	https://github.com/lmcinnes/umap
limma	Smyth et al., 2005	https://bioconductor.org/packages/release/bioc/html/limma.html
scVelo	Bergen et al., 2020	https://scvelo.readthedocs.io/
velocity	La Manno et al., 2018	http://velocity.org/velocity.py/index.html#
STARsolo	Dobin et al., 2013	https://github.com/alexdobin/STAR/blob/master/docs/STARsolo.md
Shiny	Rstudio	https://www.shinyapps.io/
SEQUEST	Sage-N Research Inc.	https://proteomicsresource.washington.edu/protocols06/quest.php
Peptide/Protein prophet v.4.02	Nesvizhskii et al., 2003	http://proteinprophet.sourceforge.net/index.html
QTools	Brill et al., 2009	N/A
ProLuCID	Xu et al., 2006	https://www.manula.com/manuals/ip2/ip2/1/en/topic/7-1-prolucid-search-engine
DTASelect	Tabb et al., 2002	https://www.scripps.edu/cravatt/protomap/dtaselect_instructions.html
Census	Park et al., 2008	http://fields.scripps.edu/yates/wp/?page_id=824
Ontologizer	Robinson et al., 2004	http://ontologizer.de/
SAINT	Choi et al., 2011; Teo et al., 2014	http://saint-apms.sourceforge.net/Main.html
DAVID	Huang et al., 2009	https://david.ncifcrf.gov/
Other		
UC7 ultramicrotome	Leica	N/A
Talos L120C TEM	Thermo Fisher Scientific	N/A
EASY-nLC 1000 Liquid Chromatograph	Thermo Fisher Scientific	Cat#LC120
Acclaim PepMap 100 C18 HPLC Columns	Thermo Fisher Scientific	Cat#164941
Exactive Plus Orbitrap Mass Spectrometer	Thermo Fisher Scientific	Cat#IQLAAEGAAPFALGMBCA

RESOURCE AVAILABILITY

Lead contact

Requests for further information, resources and reagents should be directed to and will be fulfilled by the lead contact, Nenad Sestan (nenad.sestan@yale.edu).

Materials availability

All plasmids and the lentivirus generated in this study are available from the Lead Contact without restriction. The Mettl7b mutant mice line generated is preserved as frozen sperm and will be available upon request. Reagents used in the study were of general use and from commercial sources.

Data and code availability

- Supplement contains transcriptome analysis and proteomic data with analysis. RNA-seq data is deposited at <http://www.psychencode.org/>, <https://biccn.org/data> and NCBI GEO: [GSE186538](https://www.ncbi.nlm.nih.gov/geo/query/acc.cgi?acc=GSE186538). The data can also be interactively visualized at: <http://resources.sestanlab.org/hippocampus>.
- All scripts are available at Github repository <https://github.com/sestanlab/Hippocampus>.
- Any additional information required to reanalyze the data reported in this work paper is available from the Lead Contact upon request

EXPERIMENTAL MODEL AND SUBJECT DETAILS

Human, rhesus macaque and pig postmortem tissue

Human samples were obtained from the collections of the Sestan and Rakic laboratories and from Javier DeFelipe's collection in the Instituto Cajal in Madrid (Spain). Rhesus macaque and pig brain specimens were obtained from the tissue collection of the Sestan and Rakic laboratories. All clinical histories, tissue specimens, and histological sections were evaluated to assess for signs of disease, injury, and gross anatomical and histological alterations.

Fresh tissue specimens for histology were fixed with 4% paraformaldehyde/PBS followed by 30% sucrose/PBS. No obvious signs of neuropathological alterations were observed in any of the human, macaque or pig specimens analyzed in this study. The postmortem interval (PMI) was defined as hours between time of death and time when tissue samples were fresh frozen or started to undergo fixation process.

Frozen archival tissue human specimens were used for snRNA-seq. No obvious signs of neuropathological alterations were observed in any of the specimens considered and analyzed in this study. For all other specimens, regions of interest were sampled from frozen tissue slabs or whole specimens stored at -80°C . To ensure consistency between specimens, all dissections from the same species were performed by the same person. Frozen tissue slabs were kept on a chilled aluminum plate during dissections. EC and four hippocampal subregions (DG, CA 2-4, CA1, and Sub) were microdissected as previously reported (Kang et al., 2011) from fresh frozen post-mortem human brains previously cut into 1-cm thick serial, coronal sections, and snap frozen in isopentane (J. T. Baker).

All human (*Homo sapiens*) brain specimens used for snRNA-seq transcriptome and DCX immunostaining (Tables S1 and S3) were de-identified and collected from clinically unremarkable donors and one case that died in status epilepticus. Tissue was collected following the guidelines provided by the Yale Human Investigation Committee (HIC) for the Sestan and Rakic collection or by the European Union for DeFelipe's samples from Spain. Tissue was collected and handled in accordance with ethical guidelines and regulations for the research use of human brain tissue set forth by the NIH (<http://bioethics.od.nih.gov/humantissue.html>) and the WMA Declaration of Helsinki (<https://www.wma.net/en/30publications/10policies/b3/index.html>). Appropriate informed consent was obtained and all available non-identifying information was recorded for each specimen.

The brain tissue samples of Alzheimer disease were sourced from 4 biobanks, with Braak stage II-VI and/or CERAD confirmed neuropathologic diagnosis and the PMI span 8-28 hours (Table S7).

All studies using non-human primates and pigs were carried out in accordance with a protocol approved by Yale University's Committee on Animal Research and NIH guidelines. Rhesus macaque (*Macaca mulatta*) brain samples were collected postmortem from 7 adult specimens (Tables S1 and S3). Pig brain samples were collected postmortem from 18 young adult specimens (Tables S1 and S3).

METHOD DETAILS

Anatomical definition of sampled subregions of the hippocampal formation and entorhinal cortex

The dentate gyrus (DG) was sampled from the posterior part of the anterior third of the hippocampal formation. It included all three layers: molecular, granular, and polymorphic. The deeper part of the hilus of the DG was dissected as part of the proximal portion (nearer DG) of the CA2-4 region.

Cornu Ammonis (CA) 2-4 region was sampled after DG was dissected and contained the remaining hilus containing CA4 and the proximal hippocampal fields CA3 and CA2 (until approximately the CA1 region), including all three layers: molecular, pyramidal and stratum oriens.

CA1 region (Sommer's sector) was sampled from approximately the border of CA2 to the subiculum, comprising the most distal (from the DG) portion of cornu Ammonis. The border between CA1 and CA2 is difficult to reliably identify and thus small pieces of the neighboring CA2 and, vice versa, could have been occasionally present in the samples.

The subiculum (Sub) is part of the subicular complex (subiculum, presubiculum and parasubiculum) located between the hippocampus and EC. Our sample was taken adjacent to CA1, corresponding to the subiculum, and was composed of the molecular, pyramidal and polymorphic layers and the superficial region of underlying white matter.

The entorhinal cortex (EC) spreads over both the gyrus ambiens and a considerable part of the parahippocampal gyrus. The EC samples were collected from the middle portion of the parahippocampal gyrus of the same tissue slab used to dissect the subregions of the hippocampal formation, corresponding to the proper entorhinal subregion and Brodmann area 28. The EC was also defined by presence of numerous wart-like elevations (verrucae hippocampi) on the surface of the gyrus. Samples contained all cortical layers and the superficial region of underlying white matter.

Brain cell nuclei isolation

The brain cell nuclei were isolated according to our previous protocol (Li et al., 2018; Zhu et al., 2018) with some modifications. Hippocampal regions (DG, CA1, CA2-4, Sub) and adjacent entorhinal cortex were dissected from three frozen adult human brains (Table S1). In order to avoid experimental bias and evenly dissociate the tissue for cell nuclei isolation, whole tissue was finely pulverized to powder in liquid nitrogen with mortar and pestle (Cooresk #60316, #60317). All buffers were ice cold and all reagents used for

consequent nuclear isolation were molecular biology grade unless stated otherwise. 5 - 10 mg of pulverized tissue was added into 5 mL of ice-cold lysis buffer consisting of 320 mM sucrose (Sigma #S0389), 5 mM CaCl₂ (Sigma #21115), 3 mM Mg(Ace)₂ (Sigma #G3052), 10mM Tris-HCl (pH 8) (AmericanBio #AB14043), protease inhibitors w/o EDTA (Roche #11836170001), 0.1 mM EDTA (AmericanBio #AB00502), RNase inhibitor (80U/ml) (Roche #03335402001), 1mM DTT (Sigma #43186), and 0.1% TX-100 (v/v) (Sigma#T8787). DTT, RNase Protector, protease inhibitors, and TX-100 were added immediately before use. The suspension was transferred to Dounce tissue grinder (15ml volume, Wheaton #357544; autoclaved, RNase free, ice-cold) and homogenized with loose and tight pestles, 30 cycles each, with constant pressure and without introduction of air. The homogenate was strained through 40 um tube top cell strainer (Corning #352340) which was pre-wetted with 1ml wash buffer: (250 mM sucrose (Sigma #S0389), 25 mM KCl (Sigma #60142), 5mM MgCl₂ (Sigma #M1028), 20mM Tris-HCl (pH 7.5) (AmericanBio #AB14043; Sigma #T2413), protease inhibitors w/o EDTA (Roche #11836170001), RNase inhibitor (80U/ml) (Roche #03335402001), 1mM DTT (Sigma #43186)). Additional 4 mL of wash buffer was added to wash the strainer. Final 10 mL of solution was mixed with 10 mL of 50% Optiprep (Axis-Shield# 1114542) solution (50% iodixanol (v/v), 250 mM sucrose (Sigma #S0389), 25 mM KCl (Sigma #60142), 5mM MgCl₂ (Sigma #M1028), 20mM Tris-HCl (pH 7.5) (AmericanBio #AB14043; Sigma #T2413), protease inhibitors w/o EDTA (Roche #11836170001), RNase inhibitor (80U/ml) (Roche #03335402001), 1mM DTT (Sigma #43186)) by inverting the tube 10x and carefully pipetted into 2 centrifuge tubes (Corning #430791). The tubes were centrifuged at 1000 g, for 30 min at 4°C on centrifuge (Eppendorf #5804R) and rotor (Eppendorf #S-4-72). Upon end of centrifugation, the supernatant was carefully and completely removed and total of 5 mL of resuspension buffer (250 mM sucrose (Sigma #S0389), 25 mM KCl (Sigma #60142), 5mM MgCl₂ (Sigma #M1028), 20mM Tris-HCl (pH 7.5) (AmericanBio #AB14043; Sigma #T2413), protease inhibitors w/o EDTA (Roche #11836170001), RNase inhibitor (80U/ml) (Roche #03335402001), 1mM DTT (Sigma #43186)) was added carefully on the pellets in tubes and centrifuged at 1000 g, for 10 min at 4°C on the same centrifuge and rotor. Supernatants were then carefully and completely removed, pellets were gently dissolved by adding 100 ul of resuspension buffer (see above) and pipetting 30x with 1ml pipette tip, pooled and filtered through 35 um tube top cell strainer (Corning #352340). Finally, nuclei were counted on hemocytometer and diluted to 1 million/ml with sample-run buffer: 0.1% BSA (Gemini Bio-Products #700-106P), RNase inhibitor (80U/ml) (Roche#03335402001), 1mM DTT (Sigma #43186) in DPBS (GIBCO #14190). Some DG nuclei samples (HSB179, HSB181, HSB282 and RMB3; [Table S1](#)) were fixed with methanol (American Bio AB#09110). At the end of nuclei isolation, four volumes of methanol (-20°C) were added dropwise, while mixing the nuclei suspension (final concentration: 80% methanol). The methanol-fixed nuclei were kept on ice for 15 min and then stored at -80°C. For rehydration nuclei were placed on ice, centrifuged on the same centrifuge and rotor as above - at 3000 g, 10 min at 4°C, resuspended in modified sample-run buffer (1% BSA), centrifuged at 1000 g, for 10 min at 4°C, resuspended in sample-run buffer, and prepared for 10x Genomics assay as indicated above.

Single nucleus microfluidic capture and cDNA synthesis

The nuclei samples were placed on ice and taken either to Yale Center for Genome Analysis core facility or processed in the laboratory within 15 minutes for snRNA-seq with targeted nuclei recovery of 10000 nuclei, respectively, on microfluidic Chromium System (10x Genomics) by following the manufacturer's protocol (10x Genomics, CG000183_Rev_A), with Chromium Single Cell 3' GEM, Library & Gel Bead Kit v3, (10x Genomics #PN-1000075) and Chromium Single Cell B Chip Kit (10x Genomics #PN-1000074), Chromium i7 Multiplex Kit (10x Genomics #PN-120262) on Chromium Controller (10x Genomics). Due to limitations imposed by source RNA quantity, cDNA from nuclei was amplified for 14 cycles.

Single nucleus RNA-seq library preparation

Post cDNA amplification cleanup and construction of sample-indexed libraries and their amplification followed manufacturer's directions (10x Genomics, CG000183_Rev_A), with the amplification step directly dependent on the quantity of input cDNA.

Sequencing of libraries

In order to reach sequencing depth of 20000 raw reads per nucleus, single nucleus libraries were run using paired end sequencing with single indexing on the HiSeq 4000 platform (Illumina) by following manufacturer's instructions (Illumina; 10x Genomics, CG000183_Rev_A). To avoid lane bias, multiple uniquely indexed samples were mixed and distributed over several lanes.

Single nuclei expression quantification and quality control

We quantified the expression levels of genes in each potential nucleus represented by a cellular barcode using the 10X Genomics Cell Ranger pipeline (version 3.0.2). For the human samples, reads were mapped to human reference genome GRCh38 (Ensembl release 98) and quantified in units of Unique Molecular Identifiers (UMIs) based on the combined exon-intron human annotation. Same strategies were applied to macaque and pig except that genome assembly Mmul10 and susScr11 were used for rhesus macaque and pig, respectively. Associated NCBI RefSeq gene annotations of pig and rhesus macaque were downloaded from UCSC genome browser. We took advantage of the enhanced cell-calling methodology in Cell Ranger to distinguish true cells from damaged or empty droplets. Specifically, RNA content distribution of each barcode was compared to the background concentration which was generalized from extremely low RNA-containing barcodes, and was subsequently classified as damaged if comparable profiles were seen. To further rule out low-quality cells, we excluded nuclei with mitochondrial content greater than 10%. This loose criterion was set as we aimed to incorporate certain cell types into analyses such as endothelial cells which were shown to be prone to high

mitochondrial content (Velmeshev et al., 2019). Additional filtering procedure was performed after clustering and low-dimensional embedding (see below) to eliminate cell clusters collectively displaying elevated mitochondrial and ribosomal gene expression and showing no signals of reasonable cell types.

Normalization, dimensionality reduction and clustering

We normalized the raw UMI counts using the ‘NormalizeData’ function in the R package Seurat with the scaling factor equal to 10,000 (Butler et al., 2018). To position all nuclei in a two-dimensional representation reflecting their transcriptomic similarities (Figures 1B–1D), the top 2,000 highly variable genes were obtained by the Seurat function ‘FindVariableFeatures’ with the default variance stabilizing process. We further integrated nuclei from a given species on the basis of the summarized anchor features via the function ‘IntegrateData’ and embedded ensuing nuclei in the PCA dimensions followed by Uniform Manifold Approximation and Projection (UMAP) visualization (Becht et al., 2018). To cluster nuclei according to their nearest transcriptomic neighbors, we searched for shared nearest neighbors (SNN) in the PCA space with the neighbor number being 25 and optimized the graph modularity using the Seurat function ‘FindClusters’. In general, we performed an iterative removal-clustering approach to remove nuclei with high mitochondrial or ribosomal contents and without clear cluster-related markers followed by re-clustering of the remaining nuclei. Moreover, cells and clusters co-expressing combinatory of major cell-type (ExN, InN, Astro, OPC, Oligo, immune and Vas) signatures were manually marked as doublets and excluded from the downstream analytical flow. Lastly, we re-embedded cell types of interest (i.e., ExN, InN and NNC) in the PCA space and re-clustered them using the same procedure as mentioned above, as this would offer finer details into the cell types we sought to probe into.

Tree construction

To explore the taxonomic relationships among all cell subtypes, we constructed a hierarchical tree by first averaging the gene expression levels across cells of the same subtype. The derived expression was standardized to mean of zero and variance of one within each subtype across the anchor genes selected in the previous integration step. Following this step, we calculated the Euclidean distances between pairwise subtypes, and clustered these subtypes in a structured tree (Figure 1E) by the ‘hclust’ function in R with the method set to ‘ward.D2’.

Relative cell cluster contribution from subregions and donors

Because of the absolute ratio of donors or subregions in each cluster can be biased by the differences of sample size as well as the subregions dissected in each donor, we used relative ratio instead to measure the contribution of donors or subregions to cells clusters. Specifically, we calculated the absolute ratio of a given cluster in each donor or subregion and divided this ratio by the sum of ratios across all subregions or donors. Results are visualized in Figure 1E.

Global across-dataset comparison

We performed global comparisons with two previous human HIP single nuclei RNA-seq datasets (Habib et al., 2017; Ayhan et al., 2021). We calculated the average log-transformed expression of the highly variable genes across all clusters and then performed Pearson correlation to demonstrate the subtype-subtype similarity across datasets, which were further displayed in gradient heatmaps (Figures S1G and S1H). Because the annotated neural stem cell cluster in the pioneer HIP data actually represents an ependymal cell cluster (Sorrells et al., 2021), we updated the cluster label accordingly.

Classification of cell subtypes in human

We grouped cell clusters with strong signals of *SLC17A7* expression into ExN. Furthermore, we categorized them into different subtypes through marker gene expression and comparisons with published datasets (Figures S1G and S1H; Cembrowski et al., 2016a; Cembrowski et al., 2016b; Habib et al., 2017; Cembrowski et al., 2018; Li et al., 2018; Hodge et al., 2019; Ayhan et al., 2021). Specifically, granule cells were characterized by the predominant composition of DG nuclei and prominent expression of *PROX1*. Mossy cells were described by the principal origin from DG and exclusive expression of *ADCYAP1*. We initially identified three granule cell subtypes characterized by the high expression of *SGCZ*, *PDLIM5* and *EGR1*, respectively. Given that the *EGR1*-expressing subtype is solely contributed by one donor, which are most likely caused by batch effects rather than true biological variations, it was merged to the most similar cluster, *SGCZ*-expressing subtype. ExN from CA fields were arranged mainly according to subfields: CA3 pyramidal neurons (co-expression of *CFAP299* and *SYN3*), CA2 pyramidal neurons (co-expression of *CFAP299* and *HGF*), dorsal CA1 pyramidal neurons (co-expression of *GRIK1* and *GRM3*), and ventral CA1 pyramidal neurons (co-expression of *ACVR1C* and *SYT13*). For the Sub ExN, we categorized them into three subtypes: one distal (away from CA1) (*FN1+*) subtype and two proximal ones (*ROBO1+*). Of note, the spatial registrations of CA and Sub cell subtypes were achieved on the basis of previous transcriptomic studies of hippocampal pyramidal neurons (Cembrowski et al., 2016a; Cembrowski et al., 2016b, 2018). With regards to entorhinal ExN, we classified them by two means. First, we aligned them with ExN from single nucleus data of human MTG using the same procedure as described above. Second, we examined the subtype-specific marker genes in both our ExN and related literature reports. Specifically, two layer 2 subtypes were classified as *RELN+* and one as *CALB1+* (Witter et al., 2017). Other upper-layer subtypes were depicted based on marker gene expression of *LAMA3*, *PDGFD*, *IL1RAPL2*, and *PCP4* (Ramsden et al., 2015; Tang et al., 2015; Ohara et al., 2018). The middle-to-deep layer subtypes were delineated by the specific gene expression of *RORB*, *THEMIS*, *ADRA1A*, and *TLE4*.

Cell clusters showing high GAD1 expression were then assigned as InN. InN clusters were first classified to major groups based on the expression of three canonical function markers (*PVALB*, *SST*, *VIP*) as well as *LAMP5*, a marker mostly representing a group of neurogliaform InN and recently being adopted as a major InN marker (Tasic et al., 2018; Hodge et al., 2019). For a given cluster expressing two markers simultaneously (e.g., InN *LAMP5* *NMBR* cluster expresses both *SST* and *LAMP5*), it was assigned to the same major group of the neighboring cluster in the hierarchical tree. Additionally, we used *LHX6* (a medial ganglionic eminence marker) and *NR2F2* (a caudal ganglionic eminence marker) to classify the rest of the InN clusters which do not express these markers. Finally, each InN cluster was named after the combination of major group marker (e.g., *SST*, *VIP*) and one top subtype marker (e.g., *ANO2*). Apart from these InN clusters, we also identified a *MEIS2*-expressing InN cluster corresponding to the white-matter residing InN type described before (Frazer et al., 2017; Tasic et al., 2018) and a neuron cluster co-clustered with InN showing strong signals of *RELN*, *NDNF*, highly indicative of Cajal Retzius cells.

The remaining nuclei were collectively referred to as NNC. We classified these nuclei into four big groups based on marker gene expression of *SOX10* (oligodendrocyte lineage-related cells), *AQP4* (astrocytes), *PTPRC* (immune cells) and *RGS5* (endothelial cells) (Figures S2E and S2F). The first group was further subdivided by the expression of *PDGFRA* (oligodendrocyte precursor cells, OPCs), *GPR17* (committed oligodendrocyte precursor cells, COPs), and *MOBP* (oligodendrocytes). We additionally grouped OPCs and oligodendrocytes into specific subtypes according to the high expression of specific genes: *EGR1* and *GRIA4* for OPCs; *CPXM2*, *SLC5A11*, *LINC01098* and *LAMA2* for oligodendrocytes. For astrocyte subtype specification, we classified them by the laminar distribution: *GFAP*⁺ ones located in deep layers and *CHRD1L1*⁺ ones in upper layers (Lanjakornsiripan et al., 2018). Regarding immune cells, we used marker genes *C1QB*, *F13A1*, *LYZ* and *SKAP1* to deconstruct them into microglia, macrophages, myeloid cells and T cells, respectively. Microglia were further subdivided via specific gene expression of *P2RY12* and *CD83*. In terms of vasculature lineage, we employed combinational expression of genes to sort them into arterial endothelial cells (*DKK2*⁺), endothelial cells (*CLDN5*⁺ and *VWF*⁺), pericytes (*CLDN5*⁺ and *ABCC9*⁺), venous smooth muscle cells (*ABCC9*⁺ and *P2RY14*⁺), arterial smooth muscle cells (*ACTA2*⁺ and *TAGLN*⁺) and vascular and leptomeningeal cells (*COL1A2*⁺ and *COL1A1*⁺) (Vanlandewijck et al., 2018).

Most of clusters identified are shared across donors while certain exhibited minimal or even no representation in some of the donors (Figure 1E). Among those disproportionally distributed clusters, two clusters, CR *RELN* *NDNF* and InN *SST* *NPY*, only account for 0.01%–0.02% of the cell population and were more prone to show disproportional distribution. Another interneuron subtype “InN *PVALB* *PLCL1*,” which exhibits certain level of depletion in HIP as compared to EC (Figure 1E), is also absent in a donor where only DG region was dissected. All the EC ExN subtypes were exclusively contributed by EC and were missing in the donors where only DG regions were dissected. Additionally, we observed one cluster “T *SKAP1* *CD247*” absent in one donor, probably reflecting variations of immune response across donors.

Classification of cell types in pig and rhesus macaque

The cell identity classification of pig and macaque were carried out using the same procedures as described above with a few exceptions. The annotation of nIPC and neuroblast was based on two criteria, expression of canonical cell type markers (nIPC: *MKI67*, *CENPF*, *TOP2A*; neuroblast: *DCX*, *CALB2*, *PROX1*) and clustering with mouse progenitors and neuroblast cells when integrated with mouse data. Due to the scarcity of RGL cells in pig and rhesus and their transcriptomic similarity to astrocytes, we classified those pig and macaque cells co-clustered with mouse RGL cluster as RGL cells. In total, we identified 8 and 7 RGL cells in pig (30 minutes PMI) and macaque, respectively.

Classification of cell types in fetal human hippocampus

Fetal human hippocampus cells (Zhong et al., 2020) were further subclustered using the same procedure described above to separate granule cell and pyramidal neuron differentiation lineages. Neural intermediate progenitor cells (nIPCs) were classified as *SOX2*⁺ *EOMES*⁺ *NEUROG1*⁺ and radial glia cells were annotated as *SOX2*⁺ *PAX6*⁺ *VIM*^{high} *OLIG2*^{low} *EOMES*⁻. Neuroblast cells were identified via the combinatory expression of *DCX* and *NHLH1*. Separation of DG versus non-DG ExN lineage was based on the expression of *MEIS2* (non-DG lineage) and *PROX1* (DG lineage).

Integrate dentate gyrus data across species and developmental stages

We used the same Seurat integration pipelines to integrate the DG data from mouse (Hochgerner et al., 2018), pig, rhesus macaque and human. Young adult mouse data referred to P120–P132 period of the dataset C in the original data and juvenile mouse data (P12–P35) referred to the dataset A (Hochgerner et al., 2018). Importantly, variable features were first selected via the Seurat function ‘FindVariableFeatures’ with the default variance stabilizing process for each sample and the union of highly variable genes were set as the anchor features for data integration. To more rigorously identify putative human nIPCs and neuroblasts, we applied pairwise integration between human and each of other species using both Seurat (Stuart et al., 2019) and Harmony (Korsunsky et al., 2019) harnessing the union of highly variable genes of each species pair. Here, for simplicity, we only used pig hippocampus data at 30 minutes postmortem interval for the four-species integration (Figures 2A, 2B, and S2D). Same integration pipelines were applied for the integration including human doublets (Figures S2I and S2J) as well as the integration between fetal and adult human data (Figures S2K and S2L).

RNA velocity analysis for mouse, pig, rhesus macaque and human

We first applied velocity (La Manno et al., 2018) to count the abundances of un-spliced and spliced transcripts using the bam output of CellRanger in pig, rhesus macaque and human. With regard to the mouse data (Hochgerner et al., 2018), because of the incompatibility of public sequencing files with Cellranger input, we reperformed the read alignment and UMI counting using STARsolo (Dobin et al., 2013), a tool performing similar preprocessing analysis to CellRanger, and passed the bam files to velocity package. We then applied scVelo (Bergen et al., 2020) to find variable genes, calculated RNA velocities via dynamical models and visualized the velocities on the UMAP embeddings where the four species were integrated together using the Seurat pipelines described above (Figure 2B).

Comparison of subtype markers across species and developmental stages

Subtype marker gene calculation was performed separately in each dataset using “FindMarkers” function in Seurat. We used the following strategy to minimize the marker set size bias and extrapolate the subtype similarity. Specifically, for each cluster, we checked the percentage of the top 75 markers (ranked by average fold changes) of species A present in species B markers and the percentage calculated in the reverse direction, which were then averaged to indicate the subtype similarity of the cluster between species A and B (Figure S2C).

To get cell-type specific markers that are only enriched in a given cell type, we further retained marker genes with fold changes of expression ratio no less than 1.2 and adjusted p value (Bonferroni correction) no more than 0.01. The top 20 specific markers of each subtype were then visualized in dot plots (Figure 2C). As there are insufficient RGL cells in pig and rhesus and limited nIPCs in pig, these clusters were not included in the marker analysis.

Expression profiling of *DCX* across species and regions

In order to compare the *DCX* expression across species, we down-sampled all the datasets to a comparable level. Specifically, we calculated the median of the total UMIs of the granule cell subtype in each species and computed a scaling factor using the dataset with the lowest depth. We reasoned that granule cell cluster is the best anchor given that it presents in all species with high abundance and it is a crucial part of the granule cell lineage. Then, the UMIs of each cell were subsampled to the level equal to multiplying the original library size by the scaling factor and the generated down-sampled datasets were used for the comparative analysis including *DCX* expression (Figures 3A and 3B; Table S3) and enrichment analysis (Figure 3C).

Enrichment of neurogenic marker sets in *DCX*-expressing cells

To test whether *DCX*-expressing cells show enriched expression of these neuroblast markers, we compared the area under the curve (AUC) scores of these marker sets (Aibar et al., 2017) in *DCX*-expressing and *DCX*-negative cells using Wilcoxon rank sum test (one-tailed test, Figure 3C). Gene expression ranking was first performed in each cell followed by calculation of the enrichment of the given marker set using AUC scores. Because expression ranking rather than expression level was used, the calculation was less vulnerable to expression units. We also used the down-sampled datasets to further minimize sequencing depth bias. We removed *DCX* gene from each of these marker sets prior to AUC score calculation as the presence of *DCX* in these markers could increase the AUC scores for *DCX*-expressing cells and bias the analysis.

Reanalysis of previous adult human hippocampus snRNA-seq data

We extracted the relevant cell types from a previous adult human hippocampus snRNA-seq data (Ayhan et al., 2021), which includes all the neurons, astrocytes and oligodendrocytes. Then we used the same Seurat integration pipeline described above to integrate the data from multiple batches and visualized the cell on the UMAP layout (Figure S3S). We were not able to access the cell annotations for the original Gra.Neu.5 cluster, but we found a group of granule cells corresponding to that cluster clearly marked by *LPAR1*, a marker used to label cluster Gra.Neu.5. Since we observed strong expression of all the top oligodendrocyte markers (calculated by FindMarkers function in Seurat) in this cluster (one representative marker is shown in Figure S3S), we then used AUCell (Aibar et al., 2017) to calculate the AUROC scores of oligodendrocyte markers to test their enrichment in this cluster. Doublet scores were calculated using Scrublet package (Wolock et al., 2019).

Cell subtype comparisons among HIP, EC, MTG and dIPFC

To explore the transcriptomic divergence across HIP, EC, MTG and dIPFC for all cell subtypes, we constructed a network demonstrating the relationships among the subtypes in the four brain regions based on the extent of overlap of their specific marker genes. In detail, in each region we first determined the marker genes of each subtype using the ‘FindAllMarkers’ function in Seurat. Subsequently, we generated a similarity matrix representing the overlap between marker genes of pairwise subtypes across all regions, followed by the visualization of this matrix in the form of a network via the R package ‘igraph’ through the force-directed graphopt algorithm (Figures 4B, 4D and 4F). Especially, for ExN types we displayed their connections in a between-region manner (HIP and EC, EC and MTG, and MTG and dIPFC). To further examine the cell subtype connections across different regions, in each brain region we focused on marker genes detected in at least one subtype and assessed their expression across all subtypes of remaining brain regions visualized in heatmaps (Figure S4A). Additionally, given the upper- and deep-layer marker genes identified in MTG, we calculated the percentages of genes in each subtype of each region where expression was greater than the expression constraint of 40% quantile across

all expression values (Figure S4B). Furthermore, we evaluated the expression of marker genes from intratelencephalic/intracerebral (IT) neurons and non-IT neurons of MTG in all subtypes of the four regions through first averaging the expression of each gene across cells of the same subtype and then displaying the average values across IT markers/Non-IT markers in scatterplots (Figure S4C).

Identifying genes specific to ExN of different regions

In order to identify a list of genes that exhibit enriched expression to a specific region, we first calculated the expression ratio of all the genes across all the ExN subtypes. Stringent criteria were applied to minimize the influence of technical differences across datasets. Specifically, we required the gene to have a maximum expression ratio of 0.3 across all the ExN subtypes in that region and have a minimum of fold change of 2.2 compared to the expression ratios in other regions. We also filtered genes that were prominently expressed in other regions. The region-specific genes were visualized in Figure 5B and the hippocampus ExN-specific genes were passed to the below analysis to survey their temporal specificity.

Temporal specificity of the HIP ExN-specific genes in bulk tissue transcriptomic datasets

Gene expression analysis was performed on the PsychENCODE RNA-seq datasets (Li et al., 2018). Time periods 3-15 were collapsed into three time groups: prenatal (periods 3-7), early postnatal (periods 8-12), and adult (periods 13-14). We used limma (Smyth et al., 2005) to run a regression that included the time group and brain region, as well as the region-group interactions, as factors. Genes were then ranked by the region-group coefficient differences between HIP and the maximum of other regions (Figure 5C).

Exclusive markers of cluster InN SST ADAMTS12

To find hippocampus-specific transcriptome features in the cluster InN SST ADAMTS12, we first sought to confirm the enrichment of this cluster in hippocampus by integrating InN from HIP, EC, MTG and dIPFC using the 'RunHarmony' function in the Harmony R package (Figure 5C; Korsunsky et al., 2019). Following the integration, we identified a set of markers exclusively expressed in this cluster as compared to other interneuron clusters in hippocampus and SST-expressing interneuron clusters in MTG or dIPFC. To do so, we first calculated the markers of InN SST ADAMTS12 in the hippocampal-entorhinal dataset using "FindMarkers" function in Seurat and removed those identified as marker genes in SST subtypes in MTG and dIPFC.

Generation of knockout mice and tissue processing

All experiments with mice were performed in accordance with a protocol approved by Yale University's Committee on Animal Research. Targeted embryonic stem (ES) cells (*Mettl7b*^{tm1(KOMP)Vlcg}) were obtained from Knockout Mouse Project (KOMP) repository. Chimeric mice were generated by blastocyst injection of ES cells at Yale Genome Editing Center (YGEC). Mice were bred for germline transmission to generate gene knockout mice. Genotyping was performed using the TUF/TUR primer set (145 bp) for the wild-type allele and the NeoFwd/SD primer set (351 bp) for the *Mettl7b* deletion allele.

Both wild-type and *Mettl7b* mutant mice were reared in group housing in a 12h light:12h dark cycle and provided food and water *ad libitum* with veterinary care provided by Yale Animal Resource Center. Only mice in good, healthy condition, as approved by Yale Animal Resource Center, were used for breeding and experimentation. Multiple breeding pairs were maintained and siblings were never mated to increase genetic diversity, and prevent unintended selection for features that could affect results. Both sexes were used and randomly assigned for all experiments. Adult mice were anesthetized and intracardially perfused with ice-cold PBS and 4% PFA. All mouse brain tissue specimens were fixed by immersion in 4% PFA overnight at 4 °C and sectioned at 50 μm using a vibratome (Leica).

In situ hybridization

Human brain tissue samples were fixed in 4% PFA overnight at 4 °C and sectioned at 30 μm using a Leica VT1000 S vibratome. The RNA probes complementary to human *METTL7B* cDNA (NM_152637.2) were labeled with digoxigenin-UTP (Roche). After acetylation, sections were hybridized with the probes at 63 °C for 16 hours. Following hybridization, the riboprobes were immunolabeled with anti-digoxigenin-AP conjugate and the signal was developed with NBT/BCIP overnight in dark.

Immunolabeling and histology

For METTL7B immunohistochemistry (IHC), tissue sections were pretreated with antigen retrieval with citrate buffer pH 6 at 95C for 20 mins, incubated with anti-Mettl7b antibody raised in rabbit (Atlas antibodies HPA038644; RRID:AB_2676130; 1:500) followed by ImmPRES Excel Amplified HRP Polymer Staining Kit (Anti-Rabbit IgG, MP-7601-15, Vector Laboratories) per manufacturer's protocol and using standard biotinylated secondary antibodies followed by Vectastain ABC-AP kit (AK-5000, Vector Labs) and developed with ImmPACT-DAB (SK-4105, Vector labs). For mouse α - β -galactosidase (*lacZ*) stain, tissue sections were blocked with blocking solution (5% normal donkey serum, 1% BSA, 0.1% glycine, 0.1% lysine, and 0.3% Triton X-100 in PBS) for 1 hour and incubated with primary antibodies and biotinylated secondary antibodies. The signal was amplified with Vectastain ABC-AP kit and developed with Vector Blue AP kit (SL-5300, Vector Labs) per manufacturer's protocol. DCX IHC was performed with anti-DCX antibodies raised in guinea pig (EMD Millipore AB2253; RRID:AB_1586992; 1:4000) and antibodies raised in mouse (Santa Cruz sc-271390; RRID:AB_10610966; 1:500). Immunohistochemistry for GAD1 was performed with anti-GAD1 antibody raised in goat (R&D

AF2086; RRID:AB_2107724; 1:200) and for PSA-NCAM with antibodies raised in mouse (5A5 s Hybridoma Bank; RRID:AB_528392; 1:500). All antibodies were incubated in 3% normal donkey serum, 0.25% Triton X-100 in PBS). Antigen retrieval (20 mins in citrate buffer pH 6 at 95°C) was required for optimal results with DCX and GAD1 antibodies, but not in IHC for PSA-NCAM, as it precludes it to work. Chromogenic antibody detection was achieved with biotinylated secondary antibodies, followed by ABC-AP kit and ImmPACT-DAB as described for Mettl7b. DCX controls were performed in the same way, except the primary antibody was omitted. For colocalization of DCX and GAD1, anti-guinea pig biotinylated secondary antibodies followed by Streptavidin conjugated (Jackson ImmunoResearch) antibodies were used for DCX and anti-goat secondary antibodies (Jackson ImmunoResearch) for GAD1. DAPI was used for nuclear staining. All histology samples were imaged on Aperio ScanScope system, Leica microscope, Zeiss Axio Observer with an Apotome 2 system or on a Zeiss LSM 510 confocal microscope. Cell culture samples were fixed with ice-cold 4% paraformaldehyde (PFA) for 10 minutes at room temperature, blocked for 30 minutes at RT with blocking solution (5% normal donkey serum, 1% BSA, 0.1% glycine, 0.1% lysine, and 0.3% saponin in PBS), incubated with primary and appropriate Alexa Fluor-conjugated secondary antibodies, and imaged on Zeiss LSM 510 confocal microscope.

IHC labeling for electron microscopy

Rhesus macaque brain ($n = 3$) was fixed with intracardial perfusion of 4% paraformaldehyde and 0.05% glutaraldehyde mixture. Postmortem human brain ($n = 3$) was fixed with immersion in same fixative. For antigen retrieval, vibratome 40-mm-thick slices from the hippocampus and entorhinal cortex were immersed in citrate buffer pH6 at 60°C during 20 min. Then, slices were blocked in 5% bovine albumin and incubated in rabbit METTL7B (1:500) polyclonal antibodies overnight at room temperature. For immunoperoxidase labeling, the slices were immersed in solution of biotinylated goat anti-rabbit antibodies (Jackson ImmunoResearch Inc., West Grove, PA; 1:300) and developed by the Elite ABC kit (Vector Laboratories, Burlingame, CA) with Ni-intensified 3,3'-diaminobenzidine-4HCl as a chromogen and post-fixed with 1% OsO₄. For immunogold labeling, after primary antibodies, slices were blocked in the mixture of 0.8% bovine albumin and 0.1% cold water fish skin gelatin (Aurion, Wageningen, the Netherlands). Then, slices were incubated with goat anti-rabbit IgGs conjugated with 1-nm gold particles (1:80) overnight at 4°C with subsequent silver intensification in R-Gent SE-LM kit (all from Aurion) and post-fixed with 0.5% OsO₄. Slices were dehydrated and embedded in Durcupan (ACM; Fluka, Buchs, Switzerland) on microscope slides. For electron microscopic investigations, fragments from identified hippocampal zones were re-embedded into Durcupan blocks and cut by Leica UC7 ultramicrotome into 60-nm-thick sections. Ultrathin sections were collected on one-slot grids covered with Butvar B-98 films (EMS, Hatfield, PA), stained with lead citrate, and evaluated in Talos L120C electron microscope.

Plasmids

For expression of *METTL7B*, full length cDNA (NM_152637.2) was inserted into pCAGIG (a gift from Connie Cepko, Addgene #11159) (Matsuda and Cepko, 2004). For lentiviral generation, pFUGW (a gift from David Baltimore, Addgene #14883) (Lois et al., 2002) was digested with PacI, 3' overhangs removed with Klenow (NEB) to form blunt ends, and additionally digested with BsrGI to release hUBC promoter and EGFP. The CAG-IRES-EGFP was removed from pCAGIG and ligated into pFUGW. For protein pulldown experiments, BirA-HA and HaloTag constructs were PCR-amplified from pcDNA3.1-MCS-BirA(R1 18G)-HA (a gift from Kyle Roux, Addgene #36047) (Roux et al., 2012) and pHTC-CMVneo-HaloTag (G7711, Promega), respectively, and ligated into pFUGW-CAG.

Lentiviral purification and generation of stable cell lines

Ten 15-cm dishes of sub-confluent Lenti-X 293T cells (Clontech) were used for each purification. pFUGW-CAG specific plasmids (BirA, METTL7B-BirA, HaloTag, METTL7B-HaloTag) along with pMD2.G, pRSVrev and pMDLg/pRRE (a gift from Didier Trono, Addgene #12259, #12253, #12251) (Dull et al., 1998) were transfected at 1:1:1:1 molar ratio using PolyJet (SigmaGen). Cell culture media containing lentiviral particles (LVP) was collected at 48- and 60-hours post-transfection and filtered through 0.2 μm filter to remove cellular debris. Filtered supernatants were centrifuged at 100,000 g for 2 hours. One milliliter of PBS was laid over LVP pellet and left overnight at 4°C. Next day, resuspended pellets were centrifuged through 30% sucrose gradient to further purify the virus. Lentiviral titers were determined by transducing Lenti-X 293T cells and calculating titer from FACS data between 1%–10% infection rate using formula: Titer (IU/ml) = (# cells seeded x dilution factor x % GFP-positive cells) / (volume of virus solution added).

For pulldown experiments, 50,000 ReNcell CX (EMD Millipore) cells were plated on a laminin coated 24-well plate in triplicate wells. Cells were transduced with lentiviral particles at MOI of 10 in a 150 μL of cell culture media supplemented with 10 μg/mL of protamine sulfate (#02194729, MP Biomedicals) and saved as ReN-CAG-BirA, ReN-CAG-METTL7B-BirA, ReN-CAG-HaloTag, and ReN-CAG-METTL7B-HaloTag stable cell lines.

Affinity capture of proteins

For BioID and HaloTag experiments, two million cells (ReN-CAG-BirA, ReN-CAG-METTL7B-BirA, ReN-CAG-HaloTag, ReN-CAG-METTL7B-HaloTag) were plated on four laminin coated 10-cm dishes. BioID pulldown was performed per protocol (Roux et al., 2013). At near confluency, cell culture media was supplemented with 50 μM biotin (B4639, Sigma-Aldrich). The next day, cells were rinsed twice with PBS, detached with Accutase (Millipore) for 10 minutes at 37°C, centrifuged at 200 g for 3 minutes, rinsed with PBS, and centrifuged again. Bead-protein conjugates were resuspended in 50 mM ammonium bicarbonate. HaloTag pulldown was performed per manufacturer's protocol (G6500, Promega). Proteins were eluted by resuspending HaloTag resin in 50 μL of 8 M

urea prepared in 50 mM ammonium bicarbonate and shaking for 30 minutes at room temperature. Ten percent fractions of BioID and HaloTag eluates were saved for immunoblot and silver stain analysis.

Mass spectrometry and proteomic data analysis

BioID and HaloTag tryptic digestion was performed using the optimized method from the original published method (Kim et al., 2014). Proteins were reduced by adding 2 μ L of 0.5M Tris (2-carboxyethyl) phosphine (TCEP) at 30°C for 60 min. The reaction was cooled to room temperature (RT) and proteins were alkylated in the dark for 30 min by adding 4 μ L of 0.5M Iodoacetamide. Sample volume was adjusted by adding 350 μ L of 50 mM Ammonium Bicarbonate to dilute the 8M urea to 1M before trypsin digestion. Mass spectrometry grade trypsin (Promega) was added for overnight digestion at 30°C using Eppendorf Thermomixer at 700 rpm. Formic acid was added to the peptide solution (to 2%), followed by desalting by C18 TopTip (TT10C18.96, PolyLC) and finally dried on a SpeedVac. Tryptic peptides were resuspended in 100 μ L of 2% Acetonitrile in 0.1% formic acid. Ten microliters of total tryptic peptides were used in triplicate runs for the 1D LC-MS/MS analysis, consisting of an EASY-nLC 1000 HPLC Acclaim PepMap peptide trap with a 25 cm- 2 μ m Easy-Spray C18 column, Easy Spray Source, and a Q Exactive Plus mass spectrometer (all from Thermo Fisher Scientific). A 230-min gradient consisting of 5%–16%B (100% acetonitrile) in 140 min, 16%–28% in 70 min, 28%–38% in 10 min, 38%–85% in 10 min was used to separate the peptides. The total LC time was 250 min. The Q Exactive Plus was set to scan precursors at 70,000 resolution followed by data-dependent MS/MS at 17,500 resolution of the top 12 precursors.

Protein identification and data analysis

The LC-MS/MS raw data of two technical replicates was combined and submitted to Sorcerer Enterprise v.3.5 release (Sage-N Research Inc.) with SEQUEST algorithm as the search program for peptide/protein identification. SEQUEST was set up to search the target-decoy UniProt Human Reviewed (v. March 2015) protein fasta database using trypsin for the enzyme and with the allowance of up to 2 missed cleavages, semi tryptic search, fixed modification of 57 Da for cysteines to account for carboxyamidomethylation and precursor mass tolerance of 50 ppm. Differential search included 226 Da on lysine for biotinylation (BioID samples), 16 Da for methionine oxidation, and 14, 28 and 42 Da on lysine for mono-, di- and tri- methylation. The search results were viewed, sorted, filtered, and statically analyzed by using comprehensive proteomics data analysis software, Peptide/Protein prophet v.4.02 (ISB) (Nesvizhskii et al., 2003). The minimum trans-proteomic pipeline (TPP) probability score for proteins was set to 0.9 to assure very low error (less than FDR 2%) with good sensitivity. The differential spectral count analysis was done by QTools, an open source SBP in-house developed tool for automated differential peptide/protein spectral count analysis (Brill et al., 2009) and the protein prophet peptide report was utilized to report biotinylated peptides. The LC-MS/MS raw data were also submitted to Integrated Proteomics Pipelines (IP2) Version IP2 v.3 (Integrated Proteomics Applications, Inc.) with ProLuCID algorithm as the search program (Xu et al., 2006) for peptide/protein identification. ProLuCID search parameters were set up to search the UniProt Human Reviewed (v. March 2015) protein fasta database including reversed protein sequences using trypsin for enzyme with the allowance of up to 2 missed cleavages, semi tryptic search, fixed modification of 57 Da for cysteines to account for carboxyamidomethylation and precursor mass tolerance of 50 ppm. Differential search included 226 Da on lysine for biotinylation (for BioID samples), 16 Da for methionine oxidation, and 14, 28 and 42 Da on lysine for mono-, di- and tri- methylation. The search results were viewed, sorted, filtered, and statically analyzed by using DTASelect for proteins to have protein FDR rate of less than 2.5% (Tabb et al., 2002). Differential label-free proteomics data analysis was done by IP2-Census, Protein Identification STAT COMPARE (Park et al., 2008) using two technical replicates. This result was a label-free quantification analysis, of duplicate technical data for each sample; using spectral count analysis with t test and Gene Ontology analysis (Robinson et al., 2004).

Identification of true pulldown proteins based on mass spectrometry spectral counting data

We discriminated true prey-bait interactions from false interactions in the Halotag and BioID pulldowns by using Significance Analysis of INTERactome (SAINT) method (Choi et al., 2011; Teo et al., 2014). Briefly, the SAINT method utilizes MS/MS spectral counting data and models true and false prey-bait interactions as separate Poisson distributions to obtain the probability of a true protein-protein interaction based on Bayesian statistical inference. The estimated probability provides a quantitative measure of the confidence of prey-bait interactions such that false interactions can be filtered out in a statistically-controlled manner. Upon applying the SAINT method to MS/MS spectral count data available from each pulldown experiment system, we identified 275 (out of 3 cases and 3 controls) and 1795 (3 cases and 3 controls) proteins as true METTL7B interactors from Halotag and BioID pulldowns, respectively, at Bayesian False Discovery Rate (BFDR) of 5%.

Subcellular localization of METTL7B

To characterize subcellular localization of the true METTL7B interactors, we performed fold-enrichment test for major subcellular compartments cataloged in the Human Protein Atlas database (Uhlén et al., 2015) and mammalian lipid droplet proteomes (Hodges and Wu, 2010). Human Protein Atlas provides genome-wide analysis of major subcellular localization information of human proteins based on immunofluorescent stained cells. It consists of 20 main subcellular compartments and 10,003 proteins (<http://www.proteinatlas.org>). To make the fold-enrichment test comparable across Human Protein Atlas and the mammalian lipid droplet proteome datasets, we merged the mammalian lipid droplet protein list to Human Protein Atlas dataset as a separate subcellular

localization category and used the entire Human Protein Atlas subcellular localization records uniformly as a null (background) set. We found that 73.8% (203/275) and 77.7% (1384/1795) of true METTL7B interactors from HaloTag and BioID pulldown experiments had matching HGNC gene symbols in Human Protein Atlas. Of the 152 mammalian cytoplasmic lipid proteins (Hodges and Wu, 2010), 80 proteins had matching HGNC gene symbols in the Human Protein Atlas. Twenty-three (HaloTag) and 37 (BioID) true METTL7B interactors were identified to be among 80 lipid droplet proteins in the Human Protein Atlas database.

Validation of pulldown experiments

We evaluated the performance of SAINT method by benchmarking the true METTL7B interactors against non-redundant physical BioGRID protein-protein interaction network (Stark et al., 2006). We computed the significance of interactions between proteins from the true METTL7B interactor set and the rest of the proteins (background set) in the protein-protein interaction (PPI) network by using binomial proportions test Z-score as follows (Abul-Husn et al., 2009):

$$Z = \frac{p_1/N_1 - p_2/N_2}{\sqrt{p(1-p) \cdot (1/N_1 + 1/N_2)}} \quad (\text{Eq. 1})$$

where

p_1 : number of true METTL7B interactors among the adjacent PPI network neighbors of a given protein,

p_2 : number of all the adjacent PPI network neighbors of a given protein,

N_1 : number of the true METTL7B interactors present in the PPI network,

N_2 : number of the all PPI network proteins, and

$$p = (p_1 + p_2)/(N_1 + N_2).$$

The Z-score thus provides an approximate quantitative measure of how significantly a given protein in the PPI network interacts with the true METTL7B interactors in the immediate neighborhood of the protein-protein interaction network compared to the background proteins in the protein-protein interaction network. We found that the true METTL7B interactors tend to interact much more significantly to each other than to the rest of proteins in the protein-protein interaction network (Wilcoxon rank sum test p value < 2e-16, data not shown). This indicates that the true METTL7B interactors are significantly clustered and proximal to each other in the protein-protein interaction network as expected.

KEGG pathway enrichment analysis

Toward the assessment of KEGG pathway enrichment, only these 110 high-confidence METTL7B interacting proteins reported by both strategies, were submitted to the online software, i.e., DAVID Bioinformatics Resources 6.8 (Huang et al., 2009), with the selection of “Homo sapiens” as species background and “KEGG_PATHWAY” as the targeted functional term.

Immunoblotting and silver stain

Tissue sample preparation

Tissue was lysed in PBS with 0.01% Tween-20 and protease inhibitor cocktail (P-2714, Sigma-Aldrich), and sonicated in two sessions (30 pulses at an output level of 3 using a Microson Ultrasonic Cell Disruptor [Misonix]) with 1-minute rest on ice between sessions. Samples were centrifuged at 14 000 g for 10 minutes at 4°C. Total protein concentrations were measured by the Bradford assay (#23246, Pierce).

Immunoblotting

Samples were mixed with NuPAGE LDS Loading Buffer (NP0007) supplemented with 50 mM DTT, incubated at 72°C for 10 minutes, and loaded on 4%–12% Bis-Tris gel (NP0321, Thermo Fisher Scientific). Proteins were transferred to a 0.2 μm PVDF membrane (#162-0218, Bio-Rad), blocked with 5% non-fat milk or BSA in 1% TBST buffer, and blotted with appropriate primary and secondary HRP-conjugated antibodies. The signal was developed with SuperSignal West Pico Plus Chemiluminescent Substrate (#34577, Pierce) and visualized on G:BOX Chemi XRQ (Syngene) system.

Silver stain

5% of HaloTag eluates were prepared as above and electrophoresed on 4%–12% Bis-Tris gel. Gel was processed using Silver Stain for Mass Spectrometry kit per manufacturer’s instructions (#24600, Pierce).

SAM assay

Custom made recombinant METTL7B was expressed in *E. Coli* ArcticExpress and purified from inclusion bodies by GenScript. Recombinant RTN3, RTN4, LRP1, and APP peptide were purchased directly from vendors. SAMfluoro Methyltransferase Assay (786-431, G-Biosciences) was performed per manufacturer’s instructions using ~2 μg of METTL7B and ~1 μg of substrate protein. Recombinant proteins were incubated with or without METTL7B in triplicate wells. Assay was performed at 37°C and resorufin fluorescence was measured on GloMax Multi Detection System (Promega) plate reader with an excitation wavelength of 530-540 nm and an emission wavelength of 585-595 nm.

RNA isolation and digital droplet PCR

Total RNA was extracted from human and mouse brain tissue samples, or cultured cells, using RNAeasy Plus Mini Kit (#74134, QIAGEN) per manufacturer's protocol. RNA concentrations and quality were determined using R6K ScreenTape (#5067-5576, Agilent) and TapeStation analyzer (Agilent). cDNA was synthesized from 1 μ g of total RNA using SuperScript III First-Strand Synthesis kit (#18080051, Invitrogen) and random primers. Digital droplet PCR was performed using QX200 Droplet Digital PCR (Bio-Rad) and data was normalized to *TBP* expression. PCR amplification was performed using primer sets and probes listed in [Table S6](#).

snRNA-seq profiling of human Alzheimer's disease brain middle temporal gyrus

To understand the cellular heterogeneity and disease-associated cellular changes in human AD brain, we performed unbiased massively parallel snRNA-seq with post-mortem frozen human brain tissues of middle temporal gyrus (MTG), a brain cortical region strongly affected by AD. The collection and characteristics of the AD and neurologically intact control brain samples has been described previously ([Kostylev et al., 2015](#); [Kostylev et al., 2018](#)). From 12 individuals with and without AD, we isolated brain nuclei by sucrose gradient ultracentrifugation, generated single nucleus libraries with 10x Chromium platform (10x Genomics), and sequenced on NovaSeq S4 sequencer (Illumina). We integrated snRNA-seq data of human brains from these 12 individuals of both AD (Braak Stage V/VI, n = 6) and age-matched normal controls (Ctrl, Braak Stage I/II, n = 6) by single nucleus analysis using Seurat ([Stuart et al., 2019](#)). After quality control filtering, we profiled and analyzed 64,845 single nucleus transcriptomes, clustered all the cells jointly across the 12 donors that include 6 females and 6 males, and identified and annotated the major cell types of the human brain by interrogating the expression patterns of known gene markers, including neurons (*GRIN1*), excitatory neurons (ExN, *SLC17A7*), inhibitory neurons (InN, *GAD1*), astrocytes (Astro, *AQP4*), microglia (Micro, *ITGAM*), oligodendrocytes (Oligo, *MBP*), oligodendrocyte precursor cells (OPC, *PDGFRA*), and endothelial cells (Endo, *CLDN5*). Full analysis and data will be reported elsewhere (L.Z. and S.M.S., unpublished data).

QUANTIFICATION AND STATISTICAL ANALYSIS

Differential gene expression tests, as well as the differential enrichment test of neuroblast markers, were carried out using the *wilcox.test* function implemented in R. This method does not require the assumption of normal distribution, which is appropriate for single cell data, that there is no consensus distribution model established. The related results are shown in [Figures 2C, 3C, 4B, 4E, S2G, and S3B](#). The regression of gene expression with factors including time group, brain region, as well as the region-group interactions, were performed via the R package *limma* ([Smyth et al., 2005](#)). The results are shown in [Figure 4C](#). The differential test of *METTL7B* expression in AD brains versus control brains was performed using two-tailed Fisher's exact test ([Figures S7C and S7D](#)).

In the proteomic data analysis, we identified true pulldown proteins via Significance Analysis of INTERactome (SAINT) ([Choi et al., 2011](#)), and benchmarked its acquisition using binomial proportions test detailed in a previous study ([Abul-Husn et al., 2009](#)). Gene ontology enrichment tests were performed using an online software, DAVID Bioinformatics Resources ([Huang et al., 2009](#)).

Additional statistical tests were applied to test the significance of signal differences in certain biochemical assays using the following methods: differential gene expression tests in ddPCR were carried out using one-way ANOVA with post hoc Dunnett's adjustment ([Figures 6C and 6E](#)); the signal differences in the SAM methyltransferase assay were tested using two-tailed t test ([Figure 7F](#));